Chair of Automatic Control

Technical University of Munich

Emily Lies

Modeling and System Identification of a Scaled Railway Running Gear Test Rig with Independently Rotating Driven Wheels Based on Frequency Responses

Thesis Submitted in Partial Fulfillment of the Requirements for the Degree of Bachelor of Science

at the TUM School of Engineering and Design

Supervisors: Prof. Dr.-Ing. Martin Otter
German Aerospace Center (DLR), Institute for System Dynamics and Control
PD Dr.-Ing. habil. Paul Kotyczka
Chair of Automatic Control

Advisor: Dr.-Ing. Tobias Posielek
German Aerospace Center (DLR), Institute for System Dynamics and Control

Submitted by: Emily Lies

Submission date: 03 March 2025 in Garching bei München

Erklärung

Ich versichere hiermit, dass ich die von mir eingereichte Arbeit selbstständig verfasst und keine anderen als die angegebenen Quellen und Hilfsmittel benutzt habe.

Garching bei München, den 03. März 2025  (Emily Lies)

Freiwillige ergänzende Erklärungen

☒ Mit der zeitlich unbefristeten Aufbewahrung meiner Arbeit im elektronischen Lehrstuhlarchiv erkläre ich mich einverstanden.

☐ Ich stelle die Software, die ich im Rahmen dieser Arbeit entwickelt habe, dem Lehrstuhl für Regelungstechnik unter den Bedingungen der 3-Klausel-BSD-Lizenz zur Verfügung. Ich behalte dabei die sämtlichen Urheber- sowie Nutzungsrechte und werde als Autor namentlich genannt.

Garching bei München, den 03. März 2025  (Emily Lies)

Chair of Automatic Control (Prof. Dr.-Ing. habil. Boris Lohmann)
Technical University of Munich
Boltzmannstraße 15
85748 Garching bei München
Germany

Lehrstuhl für Regelungstechnik (Prof. Dr.-Ing. habil. Boris Lohmann)
Technische Universität München
Boltzmannstraße 15
85748 Garching bei München
Deutschland

Task Description

The German Aerospace Center (DLR) is conducting internal research on the "Propulsion and Coupling" project, focusing on the drive and suspension technology of rail vehicles. As part of this, the Institute of System Dynamics and Control has a scaled (1:5) running gear test rig for testing independently rotating driven wheels as part of the “Next Generation Train” (NGT) research project. Currently, a model of the test rig based on system identification mostly based on step responses is being used.

Motivation:
So far, there has neither been an analysis of frequency responses nor an analysis of rich signals (e.g. sine sweeps). These analyses are crucial to fully understand and evaluate the behavior of the test rig in as many situations as possible. Moreover, these results would further verify the already identified parameters.

Bachelor’s thesis topic:
The goal of the bachelor’s thesis is to determine and validate the resulted system parameters based on frequency responses. The data basis for the thesis will be frequency responses of measurements of sine sweeps that have already been conducted. The frequency responses of the sine sweeps will be fitted to a linear system with regards to non-linear effects. Once the parameters have been identified, they will be verified by comparing the simulation results to measurements on the test rig.

Challenge:
As the system has shown non-linear behavior such as hysteresis or variable damping, the main challenge for the thesis will be to identify the non-linear effects in the frequency responses and evaluate whether a linear model can capture these effects accordingly.

Tasks:
- Modelling of the 1:5 NGT test rig in Matlab/Simulink
- Modelling and parameter identification of a linear model based on frequency responses
- Evaluation of the linear model with respect to occurring non-linear effects
- Verification of the model through measurements on the test rig

Supervisor at DLR:
Dr. Tobias Posielek
Tobias.Posielek@dlr.de

Professor at DLR:
Prof. Dr.-Ing. Martin Otter

Abstract

As part of the Next Generation Train (NGT) research project at the German Aerospace Center (DLR), the Institute for System Dynamics and Control is developing a new running gear concept for high-speed trains with independently rotating driven wheels (IRDWs). To investigate the running gear behavior a scaled (1:5) test rig has been developed. At present, the test rig is simulated by using a model with parameter values obtained through a system identification based on step responses.

This thesis' aim is to undertake a system identification based on frequency response to better understand the frequency-related behavior of the test rig.

The system identification is based on a state space model from prior research. In this thesis, transfer functions are derived from that model. Measurements with an input in form of a sine sweep then form the foundation to identify the parameters of the transfer functions. With this set of parameters, the parameters of the state space model are determined. The state space model is implemented in MATLAB Simulink to simulate the test rig. The results of the simulation with identified parameters are evaluated by comparing them to other measurements and sets of parameters. Following validation of the linear model, a hysteresis term is introduced to capture non-linear effects observed in the experimental data, such as oscillations not accounted for in the linear model. The parameters of the hysteresis term are also identified and evaluated.

The results demonstrate that system identification based on frequency response yields more accurate parameters for sinusoidal input simulations compared to previous approaches. Additionally, incorporating hysteresis gives the model the ability to capture non-linear effects present in the measurements, enhancing the overall fidelity of the simulation.

Kurzfassung

Im Rahmen des Forschungsprojekts Next Generation Train (NGT) des Deutschen Zentrums für Luft- und Raumfahrt (DLR) entwickelt das Institut für Systemdynamik und Regelungstechnik ein neues Fahrwerkskonzept für Hochgeschwindigkeitszüge mit mechatronischen Einzelradantrieben. Zur Untersuchung des Fahrwerksverhaltens wurde ein skalierter (1:5) Prüfstand entwickelt. Derzeit wird der Prüfstand mit Hilfe eines Modells simuliert, dessen Parameterwerte durch eine Systemidentifikation auf der Grundlage von Sprungantworten ermittelt wurden.

Ziel dieser Arbeit ist es, eine Systemidentifikation auf der Grundlage von Frequenzgängen durchzuführen, um das frequenzbezogene Verhalten des Prüfstands besser zu verstehen.

Die Systemidentifikation basiert auf einem Zustandsraummodell aus früheren Untersuchungen. In dieser Arbeit werden die Übertragungsfunktionen aus diesem Modell abgeleitet. Messungen mit einem Eingang in Form eines Sinus-Sweeps bilden dann die Grundlage für die Ermittlung der Parameter der Übertragungsfunktionen. Mit diesen Parametern werden dann die Parameter des Zustandsraummodells bestimmt. Das Zustandsraummodell wird in MATLAB Simulink implementiert, um den Prüfstand zu simulieren. Die Ergebnisse der Simulation mit den ermittelten Parametern werden durch Vergleiche mit anderen Messungen und Parametersätzen evaluiert.
Nach der Validierung des linearen Modells wird das Modell um einen Hysterese-Term erweitert, um die in den Versuchsdaten beobachteten nichtlinearen Effekte zu erfassen, wie z. B. Schwingungen, die im linearen Modell nicht berücksichtigt werden. Die Parameter des Hysterese-Terms werden ebenfalls ermittelt und evaluiert.

Die Ergebnisse zeigen, dass die auf dem Frequenzgang basierende Systemidentifikation im Vergleich zu früheren Ansätzen genauere Parameter für Simulationen mit sinusförmigem Eingang liefert. Darüber hinaus ist es durch die Einbeziehung der Hysterese möglich nichtlineare Effekte in den Messungen zu erfassen, was die Gesamttreue der Simulation erhöht.

Acknowledgments

First and foremost, I would like to express my sincere gratitude to my supervisor at DLR, Dr.-Ing. Tobias Posielek and supervisor at TUM, PD Dr.-Ing. habil. Paul Kotyczka for their invaluable guidance, continuous support, and constructive feedback throughout the course of this thesis. Their expertise, time, and dedication have been instrumental in shaping this research.

I would also like to thank the Institute of System Dynamics and Control at the German Aerospace Center (DLR) for providing the necessary resources and support, as well as for the opportunity to work on this exciting research topic.

A special thank you to Meriel, Peter, Emma, and my Mum, Adrienne, for their time and effort in proofreading this thesis.

Lastly, I am grateful to my family and friends for their unwavering support, patience, and encouragement during this journey. Their belief in me has been a constant source of motivation.

To all those who have contributed to this work in any way, I extend my deepest gratitude.

Contents

Chapter 1

Introduction

1.1 Background

The basic concept of railway running gear has not changed in decades. A typical wheelset consists of two conical, flanged wheels that are connected by a rigid axis. The key benefit of this system is its self-centering ability, even on curves . However, with this advantage comes many disadvantages. For example, this conventional running gear is responsible for high wear of the wheels and tracks [1]. Furthermore, they are loud, especially when going around curves, and the self-centering ability comes at the expense of a compromise between stability and comfort, as it limits ride comfort [2]. Hence, the current widely used concept for railway bogies has many disadvantages and further research is needed to address these fundamental challenges.

Advancements in mechatronics and control theory, especially in the field of observers, have given rise to the evolution of a new concept: Independently Rotating Driven Wheels (IRDWs). The basic concept is to remove the rigid axle between the wheels of a wheelset and to power each wheel with its own motor [3]. This allows for active steering which has the benefit of reducing noise and wear [4]. However, there are some drawbacks to this solution. Primarily, the self-centering ability is lost and has to be compensated for through control mechanisms, making the system more complex and non-linear [2].

To test the concept of a railway bogie with IRDWs the German Aerospace Center (DLR) (German: Deutsches Zentrum für Luft- und Raumfahrt) has developed a scaled railway running gear test rig [5]. Using the scaled test rig, control concepts can be developed and tested and the system dynamics of the bogie can be explored within a laboratory setting, making tests repeatable and less expensive than field tests.

Accurate mathematical models are needed to allow for simulations of the test rig and to provide a deeper understanding of its dynamics, thus enabling its subsequent control. The existing mathematical model of the rear axis of the system presented in [6] is primarily based on step responses. The objective of this thesis is to develop a model of the rear axis based on frequency responses in order to provide a deeper understanding of the frequency related dynamics of the system.

1.2 State of the Art

This chapter provides an overview of the conventional bogie concepts used in high-speed trains in Germany, the concept of IRDWs, and the Next Generation Train (NGT) project led by the DLR. Additionally, it examines ongoing research on railway bogie test rigs and introduces different forms of system identification. This review establishes the necessary background for the methodologies applied in this thesis.

1.2.1 Conventional Concept of Bogies for High-Speed Trains in Germany

A conventional railway vehicle is comprised of a vehicle body on top of two bogies with two wheelsets each [1]. The wheelsets have two wheels with conical treads, the smaller circumference being on the outside and with a flange on the inside of each wheel [2]. The wheels are connected by a solid axle, leading to a passive vehicle guidance system [1]. The passive guidance system entails passive centering of the wheelset on the tracks and the ability to go around curves without the need for active steering. When a train travels around a curve, the wheels shift on the track to a position where the outside wheel is being driven on a larger circumference than the inside wheel, leading to a higher longitudinal velocity. This is illustrated in Figure 1.1, where the black wheelset represents the wheelset on a straight track and the red dotted wheelset shows the wheels' passive steering ability on the tracks, as represented by the gray circles. To improve clarity, the flange has been omitted from the diagram.

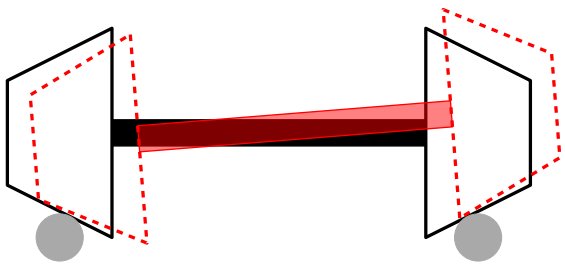

Figure 1.1: Conventional wheelset on tracks.

The main advantage of this concept is its passive centering and curving ability. Although the conventional concept is widespread and has not changed in the past decades, it has its disadvantages. The main disadvantage is high wear and loud noise when going around curves, especially tight curves, due to large creep forces [1]. Furthermore, conventional wheelsets have problems at high speeds due to the hunting oscillation [1]. One way to mitigate this motion is to connect springs from the wheelset to the bogie or vehicle body. However, this undermines its natural curving ability as it increases stiffness and can also cause severe wear of the rails and wheels [2].
The four most common bogies in European high-speed trains are the Alstom CL334, the Siemens SF500, the Bombardier Flexx Speed Italy, and the Bombardier Flexx Eco5101 [7]. The ICE4, for example, uses a variant of the Bombarider Flexx Eco as its trailing bogie and a refined version of the Siemens SF500 as its power bogie [8].

1.2.2 Independently Rotating Driven Wheels

With IRDWs each wheel has its own motor and can rotate independently. By controlling the torque of the motors, i.e. actively driving the wheel, a lateral and traction control system can be implemented [3]. If each wheel is independently driven it then becomes possible to actively drive around a curve by using different speeds for each wheel [1].
The main benefit of IRDWs over conventional wheelsets is the large reduction of rail and wheel wear, alongside a noticeable reduction of noise in curves [4]. Furthermore, IRDWs do not have an axle between them, allowing for more space in the train cars [1]; in particular, in double-decker trains. Another benefit of the use of IRDWs is that trains can be designed with their floor level at the same height as the train station platform. In addition, controlling the hunting oscillation leads to enhanced rider comfort.
Even though IRDWs have many promising advantages, there are still a number of challenges associated with them that have to be addressed. Specifically, these systems struggle to automatically return to the track's center line as they lack the longitudinal creep forces required for forward motion [3]. This gives rise to the need for a guidance system [2]. One challenge the guidance system needs to address is that the lateral displacement of the wheel-rail contact is difficult to measure due to the significant vibrations present in the environment [1, 2] and proximity to the ground. The later makes it impractical to use optical sensors due to dirt and weather conditions.
The modeling process for IRDWs is further complicated by the system's inherent uncertainty due to variations in vehicle parameters and actuator dynamics. Incorporating these dynamics would make the model excessively complex; especially given that the rail vehicle is a highly non-linear system. While simplified models are often used, these often fail to capture all dynamics [2].
Further barriers to the adoption of IRDWs are high costs, complex electronics, and the need to meet stringent safety and reliability standards [4]. IRDWs will not replace conventional wheelsets until these drawbacks, especially regarding safety standards, and the problems associated with the modeling and control of IRDWs, are convincingly addressed. This is a key driver for further research on IRDWs and a motivating factor for this thesis.

1.2.3 Next Generation Train

The Next Generation Train (NGT) is a research project that is led by DLR. It brings together multiple institutes with the objective of creating a novel double-decker high-speed train and of sharing the project's outcomes and results with those in the railway industry [9]. As part of this project, all components of a conventional high-speed train have been redesigned by nine different institutes at DLR; this includes the chassis, the wheels, and the bogie [9]. Unlike conventional double-decker trains, the two floors do not have to be interrupted above the bogies as the use of IRDWs eliminates the need for an axle between the wheels [10]. The benefits and drawbacks of IRDWs were discussed above in Subsection 1.2.2.

To test the novel running gear of the NGT, a 1:5 prototype test rig of the NGT bogie concept was developed at DLR. This is shown in Figure 1.2. Roller rigs offer the advantage of being more cost-effective than field tests; in addition, they allow for easy adjustments to the experimental setup and facilitate repeated testing [11]. The test rig has two separate wheel carriers with different stability characteristics and each wheel has

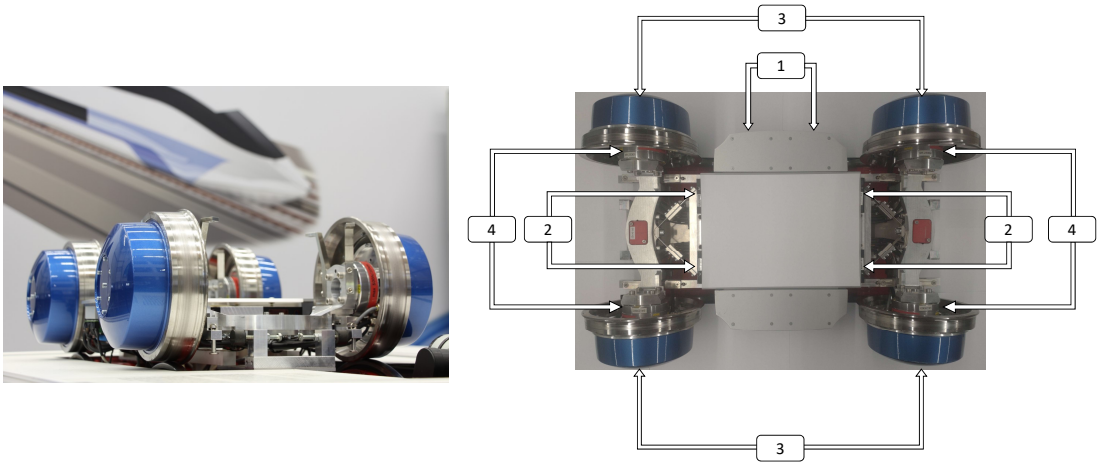

Figure 1.2: Picture of the 1-to-5 test rig at DLR and its sensor setup: (1) Laser sensors for measuring the lateral displacement; (2) Laser sensors for calculating the yaw angle; (3) Encoders for measuring the angular velocity; (4) Force torque sensors for quantifying external disturbances in [6].

a directly mounted, permanently-excited synchronous machine that acts as its motor [5, 6]. Through these motors, traction and lateral control can be achieved [10]. The wheels of each wheelset are connected by an axle bridge [6]. The bogie is placed on top of two large rollers that simulate its forward (i.e. longitudinal) motion. Furthermore, the rollers are able to manage the traction control to let the motors of the IRDWs only control the lateral displacement.

To collect data from the test rig, different sensors are installed on it. There are force torque sensors and encoders on each wheel, along with four laser sensors to measure each yaw angle and two laser sensors to measure the lateral displacement of the front and rear wheelsets [6], as shown in the right-hand image of Figure 1.2. The lasers for measuring the yaw angles are mounted onto the main frame, with each laser pointing towards the axle bridge close to a wheel. The yaw angle can then be calculated using the measured distance from the frame to the respective axle bridge. The other two lasers are mounted outside the test rig and point to two metal plates attached to the front and rear of the bogie. These provide measurements that can then be used to calculate the lateral displacement of the front and rear wheelsets on the rollers. This 1:5 test rig can be used to test various control algorithms, validate simulation models, and for the development of sensor setups [10].

1.2.4 Current Research Projects on Other Railway Bogie Test Rigs

The test rig described above is not the only such rig available for conducting research on IRDWs as there are a number of others in existence in other locations around the world. In this subsection, four of these alternate test rigs are considered and compared to the 1:5 test rig at DLR that was used to carry out the work described in this thesis. Three of these are scaled test rigs in university laboratories, while the fourth is a full scale test rig that is currently being set up at DLR as part of the NGT research project.

1:3.5 Scaled Test Rig at the Czech Technical University

The test rig located at the Czech Technical University in Prague, Czech Republic can be used to test IRDWs and conventional wheelsets [11]. This allows for direct comparisons between these two bogie concepts. It has a two-axle configuration and a scale of 1:3.5 [12]. Like the 1:5 test rig at DLR, it is also mounted on two rollers that represent the tracks. However, unlike the DLR test rig, it is also able to simulate a curved track. Furthermore, the wheels are exchangeable, which makes it possible to test wheels of different conicities. The test rig also has a system to measure wheel roller contact forces, as well as sensors to measure the displacement, acceleration, torque and force, and the forces between the axle boxes and the bogie frame.
Contact position transducers are used to measure the lateral positions of the wheelsets and measurements of the Y forces provide insights into the running dynamics of active controlled railway bogies. In addition, analysis of the wheel-rail contact forces indicates the level of wear of the wheels and rails. This test rig can be run at a revolution speed of up to 700 revolutions/min, which corresponds to a full scale vehicle speed of 230 km/h. Unlike the DLR test rig, the test rig in Prague does not have the motors directly mounted onto the wheels, rather they are located in the middle of the bogie and connected via a toothed belt, linkages, and axle boxes to the wheelsets [12].
Research carried out using this test rig mainly focuses on the application of active control in the primary suspension and wheelset guidance [12]. Furthermore, the test rig is used for torsion oscillations research and to attempt to measure adhesion of the wheel-roller contact [13].

1:10 Scaled Test Rig at the University of Tokyo

The second alternate test rig can be found at the University of Tokyo in Japan. This 1:10 test rig uses active power steering for its independently rotating wheels [11] with the goal of eliminating steering vibration and realizing close-to ideal steering. Where possible, it relies on its ability to self-steer along with a small power assist during the transition from a straight to a curved track. Like the scaled test rig at DLR, it has two wheelsets with two IRDWs each, with both primary and secondary suspension systems. It differs from the DLR rig in a number of ways. Firstly, it is at a scale of 1:10 , while DLR test rig's scale is 1:5. In addition, each wheel is connected to the frame through steering linkages, and has motors that are separate from, and not integrated into, the wheels. Furthermore, the test rig runs on scaled tracks rather than rollers. Laser displacement sensors are mounted between the axle box and the rail to measure the lateral displacement and the yaw angle [14].
Results obtained using this test rig have led to improved stability and steering utilizing a gyroscopic damper as part of the control method. This allows for passive stabilization and improvements of the dynamic behavior at high speeds [15].

1:5 Scaled Test Rig at Tongji University

The test rig at Tongji University in Shanghai, China is similar to the one at DLR in a number of ways. In particular, it has the same scale and two sets of IRDWs. However, unlike the test rig at DLR, it runs on scaled tracks with straight segments and a curve, rather than on a roller. In addition, it has both primary and secondary suspension

systems. Each wheel is connected to a subframe through an axle box, which is, in turn, connected to a subframe through primary suspension. The bogie is then connected to a subframe through secondary suspension and it contains a number of onboard devices (e.g. controllers and power inverters). In contrast to the scaled test rig at DLR, the motors are connected to the wheels through gear reducers and axle boxes, rather than being mounted directly on the wheel. In addition, the lateral displacement is also measured using two laser sensors per axis. These are mounted on the outside of the frames, below the wheels and point towards the tracks, measuring the distance from the frame to the tracks at each wheel. Additionally, like the scaled test rig at DLR, it also has laser sensors to measure the yaw angles and encoders on each wheel to measure their rotation speed [16].
This test rig is currently being used to test a data-driven multi-agent reinforcement learning controller to control active guidance. The objective of this work is to improve the running stability and reduce wheel-rail wear [16].

Full Scale Test Rig at DLR, Oberpfaffenhofen, Germany

The final alternate test rig considered is a new, full-scale test rig being developed at DLR [17]. It will enable a proof of concept for the developed NGT bogie. In particular, control concepts developed on the 1:5 test rig at DLR, as presented in Subsection 1.2.3, can be tested and validated on this full-scale test rig. As it is first and foremost a proof of concept, it only has one wheelset with two wheels and a maximum velocity of 5 m/s. Like the 1:5 test rig, and in contrast to all other test rigs considered in this subsection, the motors are directly mounted onto the wheels. It has sensors to measure forces and movements in all directions, including 20 laser displacement sensors, as well as sensors to measure force, inertia, and torque [18].

In this subsection an overview of existing test rigs for evaluation of bogie concepts with IRDWs was provided. In the following subsection the focus will move to modeling these systems and, in particular, system identification methods.

1.2.5 System Identification

System identification is a methodology used to develop mathematical models that accurately describe a dynamic system [19]. The basic steps of any system identification are as follows: First collect data about the system, then determine a model structure that will most accurately describe the system. The selected model structure is then fitted to the measurement data and finally, the identified model is then validated [20]. In this subsection, three approaches to system identification are presented.
These are system identification using learning methods, system identification based on step responses, and system identification based on frequency responses. Existing work that uses system identification based on step responses [6] serves as a reference system for the research on the system based on frequency responses detailed in this thesis.

System Identification using Learning Methods

With the advent of machine learning and super computers, the use of learning methods for system identification has received more attention in the literature or literature in

general [21]. The concept that underpins these learning methods is quite straightforward. A familiar input is given to the to-be-identified system and to a simulation model. The generated outputs of the system and of the simulation are then compared and the mathematical model underpinning the simulation is then adjusted in order to reduce the error (i.e. the differences between its output and that of the system to be identified). In this way the simulation "learns" from the error. This process is then repeated so that the simulation iteratively reduces and minimizes this error [22].
Such machine learning techniques are outside the scope of this thesis and will not be considered in this work, although they do present an interesting direction for future work.

System Identification with Step Responses

In this method of system identification, the input to the system is a step function and the response of the system to this input is the step response. This response has certain characteristics depending on the system to be identified [19]. This method of system identification has the advantage of using a very simple input signal that can easily be implemented and analyzed using a number of different methods [23]. One of the oldest amongst these is that introduced by Karl Küpfmüller in [24]. This formed the basis for the development of subsequent methods. The form of the step response enables the structure of the model to be determined and, hence, the transfer function can be found [23].

System Identification based on Frequency Responses

This method of system identification is an indirect approach [25] that involves the collection of frequency response data, from which Bode diagrams are created. Bode diagrams will be discussed in more detail in Section 2.1. A mathematical formula for the transfer function of the input to output behavior is then determined; this depends on the type of model structure used and the form of the Bode diagrams. From these diagrams of the measurement data, the parameters of the transfer function can be determined. The parameters of the fitted function can then be used to identify the parameters of the system as a whole. The great advantage of using frequency responses is their input-output behavior within a linear system: A sinusoidal input to a linear system will generate a sinusoidal output of the same frequency. Only the magnitude and phase of the output will differ to that of the input [26]. This makes it possible to look at changes between the input and the output by displaying them on Bode diagrams. From this diagram a transfer function that describes the system can be identified. This method of system identification is easy to apply in different scenarios, making it ideal for later test and validating work using the full-scale test rig [1]. However, there is one disadvantage to system identification through frequency responses that should be noted; namely carrying out the transformation can give rise to a loss of information. In this thesis the measurements used to carry out the system identification are those obtained using sinusoidal inputs of different frequencies.

This completes the overview of the state of the art section in relation to IRDWs, test rigs, and system identification. In the following subsection the objective of this work will be laid out.

1.3 Objective of this work

Conventional railway bogies rely on wheelsets that are coupled through a rigid axis; these create an inherently stable system, but limit the flexibility of the associated control systems. In addition, they cause high wear of the wheels and tracks, and reduce the overall ride comfort. Taken together, these disadvantages suggest the need for research into the development of new concepts for wheelsets. IRDWs offer advantages such as improved traction control and reduced wear but introduce dynamic challenges, including non-linear behavior. Scaled railway test rigs allow for the effective study of running gear dynamics. However, accurate system models are necessary to interpret their behavior adequately. The current model is mainly based on step responses, which may not fully capture the frequency-dependent characteristics of the system. Therefore, an improved methodology to model the test rig is needed to provide a more accurate method to capture the dynamic behavior of the system. In this thesis frequency response was chosen as a method of parameter identification, as it focuses on the frequency-related characteristics of the system.
To enable the identification of a more accurate model, the mathematical model of the rear axis presented in [6] was used as the basis for parameter identification. The recorded data, including yaw angles, lateral displacement, and the current input, were processed using Fourier analysis in order to prepare it for system identification. This process utilized the System Identification Toolbox (SIT) in MATLAB [27], where the input used was the frequency response of the Fourier transform of the measurement data. Additionally, the transfer functions were manually fitted. This allowed for a comparison of the SIT output and a manual fit to the measurements and made it possible to choose the set of parameters that most accurately represented the measurements. The system identification process then estimated the parameters of these transfer functions, which in turn enabled the identification of the model parameters.
Using the chosen set of identified parameters, a frequency response-based model to simulate the system was then constructed in MATLAB Simulink. To verify the accuracy of the linear model, simulation results were compared with additional measurement data. Furthermore, the identified parameters were then compared to those from an existing model, which was primarily derived from step responses [6]. To expand the model, hysteresis was introduced and evaluated. Finally, the findings of the work were summarized and suggestions for future research were made.

1.4 Structure of the Thesis

Following on from the introduction and overview of the state of the art presented above, this thesis is organized into four chapters focused on system identification of the linear model. These cover the underlying theory, the simulation work, the practical application of the model, and, finally, evaluation of the identified model. Chapter 2 introduces the mathematical model of the 1:5 test rig, based on the work detailed in [6]. It also provides an overview of the key mathematical and control theory concepts used, including transfer functions and Bode diagrams. The process of system identification is described in detail, highlighting the model parameters to be fitted and the underlying algorithms used for their identification. This leads to a discussion of the simulation approach, which is implemented using MATLAB Simulink. It shows the theoretically expected results of the model.

Following the theoretical and simulation sections, the practical application of the model is introduced in Chapter 4. It introduces the test rig setup and measurement data used. Moreover, measures taken to pre-process the measurement data for system identification are described. The system identification by the SIT is then compared to the manually found transfer function. The parameter identification of the test rig is finally presented. Chapter 5 presents an evaluation and discussion of the identified model. In particular, it compares simulation results with actual measurement data, discussing the accuracy and validity of the mathematical model and the identified parameters. It also shows measurements of sine sweeps with different amplitudes, introducing a non-linearity of the test rig. Additionally, the identified parameters are compared to those from an existing model mostly based on step responses. A discussion of the similarities and differences of the models is then provided.
To improve the model, hysteresis as a non-linear phenomenon is introduced by expanding the linear mathematical model and the simulation. The parameters of the hysteresis are manually adjusted to try to capture the measurements more accurately and the results of this parameter tuning process are then presented.
The thesis concludes with an assessment of the implications of the research and recommendations for future work.

Chapter 2

Theory Background on System Identification and Modeling

This chapter presents the fundamental concepts of frequency analysis and the frequency response of PT1 and PT2 elements. It then introduces the model utilized in this thesis, which is based on the model developed in [6, 28]. From this model, the transfer functions are derived, providing the foundation for parameter identification. The theoretical equations derived in this chapter are then applied in MATLAB Simulink simulations, as described in Chapter 3, and are also used for the experimental parameter identification process outlined in Chapter 4.

2.1 Fundamental Transforms and Frequency Analysis

As part of the process of frequency analysis, signals are often Fourier-transformed and plotted as a Bode diagram. These will be described in more detail in this section. The input signal used for the work presented in this thesis, the linear sine sweep, is then introduced. Finally, the Laplace transform is briefly outlined, as it is used when describing transfer functions.

2.1.1 Fourier Transform

With the Fourier transform a signal can be separated into trigonometric functions with a continuous amplitude spectrum [29]. One can obtain information about the magnitude and phase at every given frequency through a Fourier transform. This can then be used to create Bode diagrams. The Fourier transform is defined in [30] as

$$F(\omega) = \frac{1}{2\pi} \int_{-\infty}^{+\infty} f(t) e^{-j\omega t} \mathrm{d}t = A(\omega) e^{-j\varphi(\omega)}; \tag{2.1}$$

where $A(\omega)$ is the continuous amplitude spectrum defined as

$$A(\omega) = \sqrt{\left(\mathrm{Re}F\left(\omega\right)\right)^2 + \left(\mathrm{Im}F\left(\omega\right)\right)^2}; \tag{2.2}$$

and $\varphi(\omega)$ is the continuous phase spectrum with

$$\varphi(\omega) = \arctan \frac{\mathrm{Im}F(\omega)}{\mathrm{Re}F(\omega)}. \tag{2.3}$$

For a linear system with the input $A \sin \omega t$, the output takes the same form $\tilde{A} \sin \omega t + \varphi$. The only changes from input to output are the magnitude $\tilde{A}$ and a phase shift of φ [26]. To transform a discrete signal, the discrete Fourier transform is used, which reconstructs the full function and then performs the Fourier transform [30].

2.1.2 Bode Diagrams

A Bode diagram consists of two separate plots, one for the magnitude A and one for the phase φ [31] on the vertical scale. Both are plotted over a logarithmic scale of angular frequency ω in rad/s. The information for the magnitude A and the phase φ are obtained by Fourier-transforming the signal of interest, as explained above in Subsection 2.1.1. The magnitude A expresses the gain and is given in dB and the phase φ can either be given in radians (rad) or in degrees (°). To obtain the transfer function from input to output, the magnitude of the output is divided by the magnitude of the input and the phase of the input is subtracted from the phase of the output. The magnitudes are divided to obtain the gain, while the phases are subtracted to determine the phase shift. Examples of different Bode diagrams can be found in Section 2.2. Bode plots provide information about stability, the value of break frequencies, and the static gain. This allows the system's transfer function to be identified using only the information found in the magnitude and phase plot.

2.1.3 Linear Sine Sweep

A linear sine sweep is a signal with linear frequency modulation. The frequency of a sinusoidal signal increases linearly from a start frequency f_0 to an end frequency f_1 in the time T. The rate of change of frequency k is defined as $k = \frac{f_1 - f_0}{T}$. The signal is described in [32] as

$$s(t) = \mathrm{rect}\left(\frac{t}{T}\right) \exp\left\{j2\pi\left(f_0 t + \frac{k}{2}t^2\right)\right\}. \tag{2.4}$$

Sine signals with time-variant frequency are also referred to as chirp signals. As described in [32], the amplitude and phase spectrum of the sine sweep can be approximated if the time-bandwidth product (TBP) is larger than 100. The TBP is calculated as TBP $= T(f_1 - f_0)$. In this thesis measurements of the length $T = 150\,\mathrm{s}$ with a frequency range from $1 \cdot 10^{-3}\,\mathrm{rad/s}$ to $640\,\mathrm{rad/s}$ were used. This leads to TBP $= 15278.9$, which is significantly greater than the threshold value of 100. Therefore, only the approximated magnitude and phase of a sine sweep are needed. From [32] they were defined as

$$|G_{\mathrm{chirp}}(j\omega)| = \frac{1}{k}\mathrm{rect}\left(\frac{j\omega}{f_1 - f_0}\right); \tag{2.5a}$$

$$\angle G_{\mathrm{chirp}}(j\omega) = -\frac{\pi(j\omega)^2}{k} + \frac{\pi}{4}. \tag{2.5b}$$

Since a sine sweep measurement covers a given frequency spectrum, the amplitude A and phase φ of all covered frequencies can be directly obtained from the Fourier transform of the signal. Therefore, a Bode diagram for the frequencies covered can be created with just one measurement. This is why sine sweep measurements were used in this thesis as they are especially convenient and straightforward to use.

2.1.4 Laplace Transform

The Laplace transform as presented in [29] can be used to solve ordinary differential equations. It does so by transforming the differential equation into an algebraic expression, which can then be solved. The solution of the differential equation is then derived by using the inverse Laplace transform. The Laplace transform is defined in [30] as

$$\mathcal{L}\left\{f\left(t\right)\right\} = \int_0^\infty e^{-st} f\left(t\right) \, \mathrm{d}t = F\left(s\right). \tag{2.6}$$

The transform of a derivative is

$$\mathcal{L}\left\{y^{(n)}(t)\right\} = s^n Y(s) - \sum_{i=0}^{n-1} s^{n-i-1} y_i;$$

where y_i is the value of $y^{(i)}(0)$ at $t = 0$, as defined in [30]. The transfer functions $G(s)$ in this thesis are Laplace transformed and describe the transfer behavior from input to output as a function of s.

2.2 Frequency Response of PT1 and PT2 Elements

The equations to describe the introduced transfer behaviors from u to Ψ and from Ψ to y are of the second and first order, respectively. These will be discussed further in Section 2.4 of this chapter. In this section the general form of these transfer functions is introduced. Both are of the form of proportional blocks with lag elements of first or second order [33].

2.2.1 PT1 Element

A PT1 element is a proportional element with a first order lag with the transfer function of the standard form described in [26] as

$$G_{\mathrm{PT1}}(s) = \frac{k}{\frac{1}{\omega_\mathrm{b}} s + 1}, \tag{2.7}$$

where k is the static gain and ω_b the break frequency. To look at the transfer function in the frequency domain, s is replaced by $j\omega$. The magnitude $|G_{\mathrm{PT1}}(j\omega)|$ and the phase shift $\angle G_{\mathrm{PT1}}(j\omega)$ are described by

$$|G_{\mathrm{PT1}}(j\omega)| = \frac{|k|}{\left|\sqrt{\frac{\omega^2}{\omega_\mathrm{b}^2}+1}\right|}; \tag{2.8a}$$

$$\angle G_{\mathrm{PT1}}(j\omega) = -\arctan\left(\frac{\omega}{\omega_\mathrm{b}}\right). \tag{2.8b}$$

As shown in Figure 2.1, the Bode plot of the magnitude starts with a horizontal line at $|G(j\omega_{\min})|_{\mathrm{dB}} = 20\log(k)$ until it reaches the break frequency ω_b and from then on follows a straight line with a gradient of -20 dB/decade. The actual value of the magnitude at the break frequency ω_b is $20\log(k) - 3\mathrm{dB}$.
The phase of the Bode plot starts at 0° for zero frequency in the case of $k > 0$ and drops down to -90° for high frequencies ($\omega \to \infty$). It passes -45° at the break frequency ω_b [26].

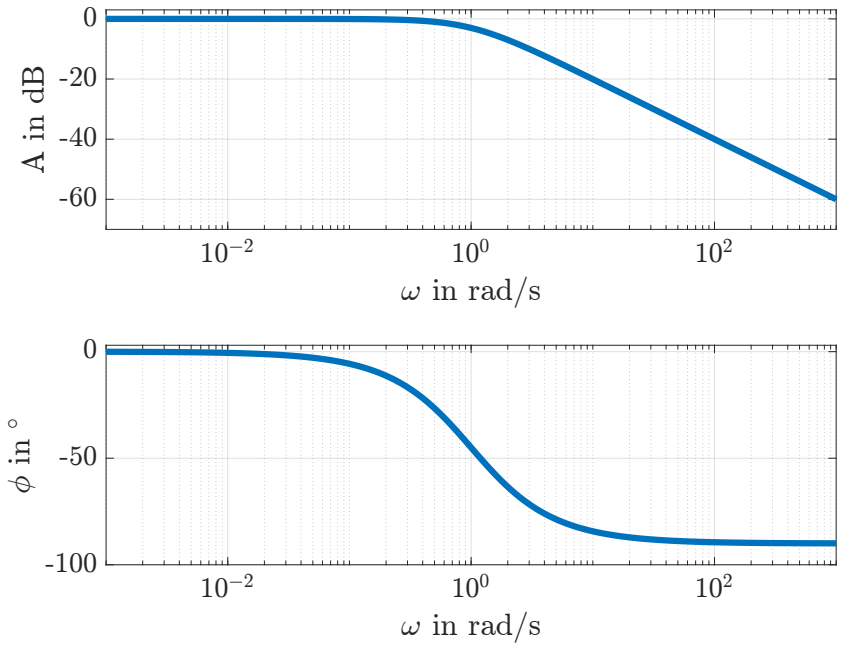

Figure 2.1: Bode diagram of a PT2 element with $k = 1$ and $\omega_\mathrm{b} = 1$.

2.2.2 PT2 Element

In [26] the standard form of a second order differential equation system is described as $\ddot{y} + 2\zeta T\dot{y} + T^2 y = T^2 k u$, with y being the output variable, u being the input variable, ζ the damping coefficient, $T = \frac{1}{\omega_\mathrm{b}}$ the inverse break frequency, and k represents the static gain. This leads to a transfer function of the form

$$G_{\mathrm{PT2}}(s) = \frac{Y(s)}{U(s)} = \frac{\omega_\mathrm{b}^2 k}{s^2 + 2\zeta\omega_\mathrm{b} s + \omega_\mathrm{b}^2}. \tag{2.9}$$

To look at the frequency response, s is again replaced with $j\omega$. As described in [26] the magnitude $|G_{\mathrm{PT2}}(j\omega)|$ and the phase shift $\angle G_{\mathrm{PT2}}(j\omega)$ are defined as

$$|G_{\mathrm{PT2}}(j\omega)| = \frac{|k|}{\left|\sqrt{\left(1-\frac{\omega^2}{\omega_\mathrm{b}^2}\right)^2 + \left(2\zeta\frac{\omega}{\omega_\mathrm{b}}\right)^2}\right|}; \tag{2.10a}$$

$$\angle G_{\mathrm{PT2}}(j\omega) = \arctan\left(\frac{2\zeta\frac{\omega}{\omega_\mathrm{b}}}{1-\left(\frac{\omega}{\omega_\mathrm{b}}\right)^2}\right). \tag{2.10b}$$

Just like the Bode plot of the magnitude of a PT1 element, the magnitude of a PT2 element starts with a horizontal line at $|G_{\mathrm{PT2}}(j\omega_{\min})|_{\mathrm{dB}} = 20\log(k)$ until it reaches the break frequency ω_b, as can be seen in Figure 2.2. At this point, the PT2 element shows different behavior to the PT1 element, depending on the value of the damping coefficient ζ. As will be introduced in Subsection 2.4.1, one of the transfer behaviors discussed in this work takes the shape of a PT2 element with $0 < \zeta < 1$. This is the oscillating case in which the two poles of the transfer function are a pair of complex conjugated values and the magnitude forms a resonance peak around the break frequency ω_b and can get very large [33]. After the resonance peak ($\omega > \omega_\mathrm{b}$), the magnitude line slopes downwards with -40 dB/decade [26].
The Bode plot of the phase shift start at 0° for $k > 0$ and ends at -180° for $\omega \to \infty$, reaching -90° at the break frequency ω_b. The smaller the damping factor ζ, the steeper the phase shifts from 0° to -180° [33].

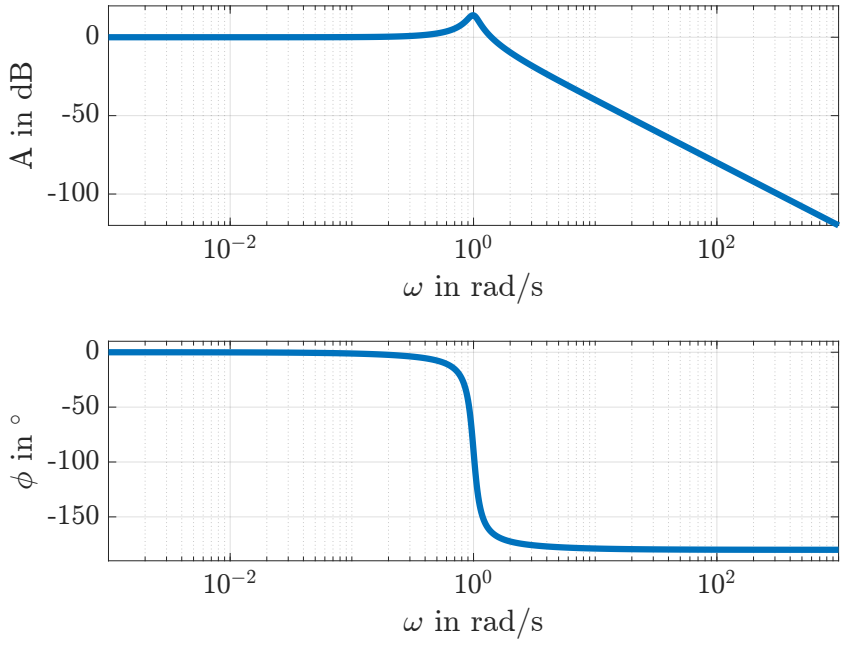

Figure 2.2: Bode diagram of a PT2 element with $k = 1$, $\zeta = 0.1$, and $\omega_\mathrm{b} = 1$.

2.3 Modeling of the 1-to-5 Test Rig

Current research on the 1-to-5 test rig at DLR focuses on improving existing models and on developing an observer to estimate the lateral displacement [6, 28]. In [28] an observer was designed, based on a class of linear systems. Furthermore, a theoretical model of the rear axis was subsequently considered with regards to non-linearities in [6]. The linear model for the rear axis, as shown in [6], has the form

$$\dot{x} = Ax + Bu. \tag{2.11}$$

In the state vector $x = \begin{bmatrix} y_\mathrm{r} & \Psi_\mathrm{r} & \dot{\Psi}_\mathrm{r} \end{bmatrix}^T + A^{-1}x_\mathrm{off}$, y_r represents the lateral displacement of the rear axis, Ψ_r represents the yaw angle of the rear axis, and $\dot{\Psi}_\mathrm{r}$ its derivative with regards to time. It is added to $A^{-1}x_\mathrm{off}$, the inverse of the system matrix A times an offset vector $x_\mathrm{off} = \begin{bmatrix} \frac{\bar{c}_y}{2l_0} v(y_\mathrm{f} + y_\mathrm{off}) & 0 & \omega_0^2 \Psi_\mathrm{off} \end{bmatrix}^T$. The input of the model is the current input u.

As this work focuses only on the rear axis of the test rig, the lateral displacement of the rear axis y_r and the yaw angle of the rear axis Ψ_r are displayed without subscripts for better readability.

The parameter $\bar{c}_y$, introduced in the vector for x_off is induced by the non-flatness of the wheel,

$$\bar{c}_y = \frac{2r_0 \cos\delta_0{}^3 - 2r_0 \cos\delta_0 + b \cos\delta_0{}^2 \sin\delta_0}{b \sin\delta_0}; \tag{2.12}$$

and dependent on the wheel radius r_0, the track width b, and the equivalent conicity δ_0. The distance between the wheel carrier and the middle frame is defined through l_0, v is the longitudinal velocity, described in Table 2.1, y_f describes the lateral displacement of the front axis, the parameter ω_0 is

$$\omega_0 = \sqrt{\frac{k_\mathrm{c}}{J_z}}; \tag{2.13}$$

including the equivalent stiffness k_c and the axle bridge inertia with regards to yawing J_z. The offset parameters y_off and Ψ_off are further described in Section 2.5 below. The system matrix A and input matrix B are as follows

$$A = \begin{bmatrix} \frac{-v\bar{c}_y}{2l_0} & v\bar{c}_y & 0 \\ 0 & 0 & 1 \\ 0 & -\omega_0^2 & -2D\omega_0 \end{bmatrix}, \qquad B = \begin{bmatrix} 0 \\ 0 \\ K\omega_0^2 \end{bmatrix}.$$

The parameters

$$D = \frac{k_\mathrm{d}}{2J_z\omega_0} = \frac{k_\mathrm{d}}{2J_z\frac{k_\mathrm{c}}{J_z}}; \tag{2.14}$$

$$K = \frac{b}{r_0 J_z \omega_o^2} k_\tau = \frac{bk_\tau}{r_0}\frac{1}{J_z\frac{k_\mathrm{c}}{J_z}} = \frac{bk_\tau}{r_0 k_\mathrm{c}}; \tag{2.15}$$

are also introduced to simplify the interpretation of the state space model. They contain the equivalent damping parameter k_d and the motor constant k_τ, as well as previously introduced parameters and constants.

This leads to

$$\begin{aligned}
x &= \begin{bmatrix} y & \Psi & \dot{\Psi} \end{bmatrix}^T + A^{-1}x_\mathrm{off} \\
&= \begin{bmatrix} y \\ \Psi \\ \dot{\Psi} \end{bmatrix} + \begin{bmatrix} -\frac{2l_0}{v\bar{c}_y} & -\frac{4l_0 D}{\omega_0} & -\frac{2l_0}{\omega_0^2} \\ 0 & -\frac{2D}{\omega_0} & -\frac{1}{\omega_0^2} \\ 0 & 1 & 0 \end{bmatrix} \begin{bmatrix} \frac{\bar{c}_y}{2l_0} v(y_\mathrm{f} + y_\mathrm{off}) \\ 0 \\ \omega_0^2 \Psi_\mathrm{off} \end{bmatrix} \\
&= \begin{bmatrix} y \\ \Psi \\ \dot{\Psi} \end{bmatrix} + \begin{bmatrix} -\frac{2l_0}{v\bar{c}_y}\frac{\bar{c}_y v}{2l_0}(y_\mathrm{f} + y_\mathrm{off}) - \frac{2l_0}{\omega_0^2}\Psi_\mathrm{off} \\ -\frac{1}{\omega_0^2}\omega_0^2\Psi_\mathrm{off} \\ 0 \end{bmatrix} \\
&= \begin{bmatrix} y - y_f - y_\mathrm{off} - 2l_0\Psi_\mathrm{off} \\ \Psi - \Psi_\mathrm{off} \\ \dot{\Psi} \end{bmatrix}.
\end{aligned} \tag{2.16}$$

One interesting thing to note about the state vector x is that the first row is dependent on Ψ_off. This is further discussed in Section 2.5 below.

The constants and parameters are presented in Table 2.1 and Table 2.2, respectively, and the sensor measurements are illustrated in Figure 2.3. It should be noted that the values of the parameters will be determined later through parameter identification.

Table 2.1: Constants for the state space model.

Notation	**Description**	**Value**	**Unit**
v	longitudinal velocity	1	m/s
r_0	wheel radius	0.1	m
b	track width	0.3	m
k_τ	motor constant	0.27	N m/A

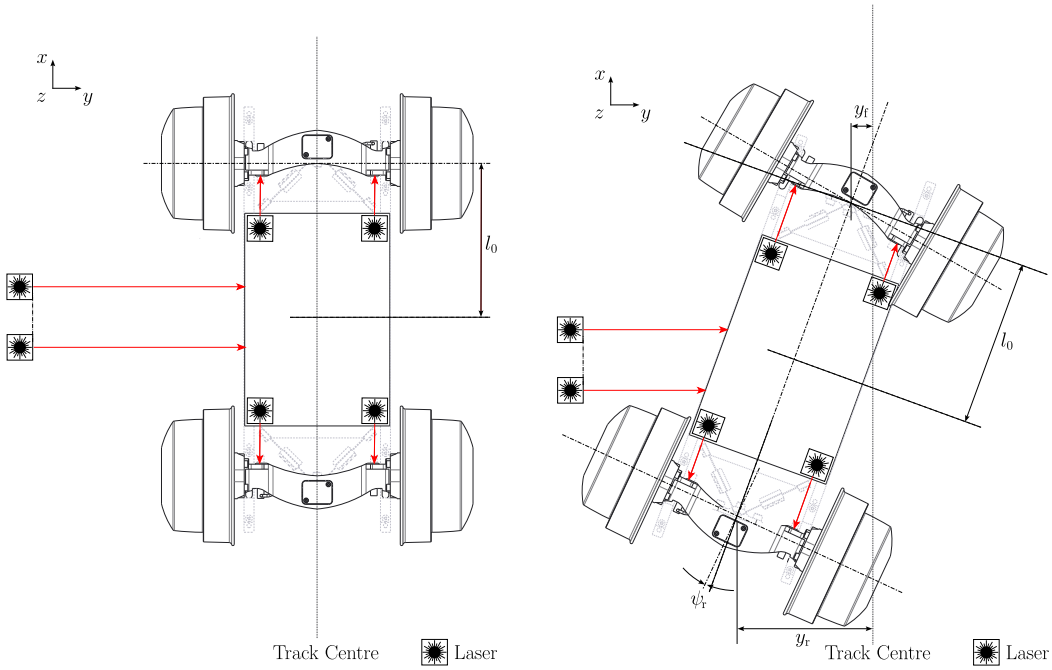

Figure 2.3: Illustrations of the test rig's laser sensors, variables and states. The red lines illustrate the direction of the laser sensors. The illustration on the left shows the nominal state without lateral displacement and yaw angle. The illustration on the right shows the change in variables for a non-zero lateral displacement and yaw angle. All quantities are highly exaggerated for clarity. Illustrations taken and customized from [6].

Table 2.2: Parameters for the state space model.

Notation	**Description**	**Unit**
l_0	distance wheel carrier and middle frame	m
δ_0	equivalent conicity	rad
y_{off}	offset lateral displacement	m
J_z	axle bridge inertia w.r.t yawing	$\text{kg}\,\text{m}^2$
k_{c}	equivalent stiffness	N/m
k_{d}	equivalent damping	$\text{N}\,\text{s/m}$
Ψ_{off}	offset yaw angle	rad

Substituting (2.16) into the state space model presented in (2.11) leads to the following expression for $\dot{x}$:

$$\dot{x} = \begin{bmatrix} \dot{y} - \dot{y}_{\text{f}} \\ \dot{\Psi} \\ \ddot{\Psi} \end{bmatrix} = \begin{bmatrix} -\frac{v\bar{c}_y}{2l_0}(y - y_{\text{f}} - y_{\text{off}} - 2l_0\Psi_{\text{off}}) + v\bar{c}_y(\Psi - \Psi_{\text{off}}) \\ \dot{\Psi} \\ -\omega_0^2(\Psi - \Psi_{\text{off}}) - 2D\omega_0^2\dot{\Psi} + K\omega_0^2 u \end{bmatrix}. \tag{2.17}$$

To avoid a Dirac delta function in the transfer function from u to Ψ, $\tilde{\Psi}$ is introduced, with $\tilde{\Psi} = \Psi - \Psi_{\text{off}}$. Hence, the third row of $\dot{x}$ (2.17) becomes

$$\ddot{\tilde{\Psi}} = -\omega_0^2\tilde{\Psi} - 2D\omega_0^2\dot{\tilde{\Psi}} + K\omega_0^2 u. \tag{2.18}$$

It should be noted that Ψ_{off} is time-invariant, meaning $\dot{\tilde{\Psi}} = \dot{\Psi}$ and $\ddot{\tilde{\Psi}} = \ddot{\Psi}$. (2.18) will be used to obtain the transfer function from u to $\tilde{\Psi}$ as shown in Subsection 2.4.1 below.

In addition, the first row of (2.17) forms the basis for the transfer function from Ψ to y as will be introduced in Subsection 2.4.2. As this model only looks at the rear axis $y_{\text{f}} = 0$, and using $\tilde{y} = y - y_{\text{off}}$, the expression for $\dot{\tilde{y}}$ becomes

$$\dot{\tilde{y}} = -\frac{v\bar{c}_y}{2l_0}\left(\tilde{y} - 2l_0\Psi_{\text{off}}\right) + v\bar{c}_y\tilde{\Psi}. \tag{2.19}$$

2.4 Transfer Functions

There are two methods to find the transfer functions. They can either be derived from the differential equation system in (2.17), or they can be found through the formula $G(s) = C(sI - A)^{-1}B$ [31], where the matrices A and B are those of the state space model (2.11) and C is the output matrix. In this section the transfer function from u to Ψ will be derived through the differential equation, while the second transfer function from Ψ to y will be obtained through the formula for $G(s)$.

2.4.1 Transfer Function from u to Ψ

The transfer function from u to Ψ can be derived from (2.18). First (2.18) has to be Laplace-transformed, leading to

$$s^2\Psi(s) = -2D\omega_0^2 s\Psi(s) - \omega_0^2\Psi(s) + K\omega_0^2 U(s);$$

which gives

$$(s^2 + 2D\omega_0^2 s + \omega_0^2)\Psi(s) = K\omega_0^2 U(s);$$

where $\Psi(s)$ is the Laplace-transformed output and $U(s)$ the Laplace-transformed input. From this the transfer function can be obtained:

$$G(s) = \frac{\Psi(s)}{U(s)} = \frac{K\omega_0^2}{s^2 + 2D\omega_0^2 s + \omega_0^2}. \tag{2.20}$$

This transfer function is of the form of a PT2 element as introduced in (2.9) with $k = K$, $\omega_{\text{b}} = \omega_0$, and $\zeta = D$ substituting (2.13) – (2.15), (2.9), and (2.20), such that

$$k = K = \frac{bk_\tau}{r_0 k_c} \Rightarrow k_c = \frac{bk_\tau}{r_0 k}; \tag{2.21a}$$

$$\omega_b = \omega_0 = \sqrt{\frac{k_c}{J_z}} \Rightarrow J_z = \frac{k_c}{\omega_b^2}; \tag{2.21b}$$

$$\zeta = D = \frac{k_d}{2J_z\sqrt{\frac{k_c}{J_z}}} \Rightarrow k_d = 2\zeta J_z\sqrt{\frac{k_c}{J_z}}. \tag{2.21c}$$

2.4.2 Transfer Function from Ψ to y

The transfer function found with $G(s) = C(sI - A)^{-1}B$ with $C = \begin{bmatrix}1 & 0 & 0\end{bmatrix}$ is the transfer function from u to y,

$$G_{\mathrm{uy}}(s) = \frac{v\bar{c}_y K\omega_0}{\left(s + \frac{v\bar{c}_y}{2l_0}\right)\left(s^2 + 2D\omega_0 s + \omega_0^2\right)}. \tag{2.22}$$

$G_{\mathrm{uy}}(s)$ can then be divided by the transfer function from u to Ψ, presented previously in Subsection 2.2.2, to receive the overall transfer function [31]. Consequently, the transfer function from Ψ to y is

$$G_{\Psi\mathrm{y}}(s) = \frac{G_{\mathrm{uy}}(s)}{G_{\mathrm{u}\Psi}(s)} = \frac{v\bar{c}_y}{s + \frac{v\bar{c}_y}{2l_0}}. \tag{2.23}$$

The parameters l_0 and δ_0 can be identified from this transfer function. As δ_0 is part of trigonometric functions of higher orders in the equation for $\bar{c}_y$ (2.12), it will be numerically estimated using the Newton method as described in [29]. Comparing the form of the transfer function for PT1 elements (2.7) with (2.23) yields

$$k = 2l_0 \Rightarrow l_0 = \frac{k}{2}; \tag{2.24a}$$

$$\omega_b = \frac{\bar{c}_y v}{2l_0} \Rightarrow \bar{c}_y = \frac{2l_0\omega_{\mathrm{b}}}{v}. \tag{2.24b}$$

To identify δ_0, (2.12) has to be rearranged into the form $f(\delta_0) = 0$ where

$$f(\delta_0) = \frac{(2r_0\cos{\delta_0}^3 - 2r_0\cos\delta_0 + b\cos{\delta_0}^2\sin\delta_0)v}{b\sin\delta_0} - \frac{2l_0\omega_{\mathrm{b}}}{v}. \tag{2.25}$$

To solve this equation the MATLAB function `fzero` [34] is used, which is based on an algorithm found in [35]. It finds the nearest value of x to a starting value where the function has a sign change. In this case the starting value is assumed to be $x_0 = 2.4 \cdot 10^{-2}\,\mathrm{rad}$, as this is the nominal value presented in [6].

2.5 Offset Parameters

In the model presented in (2.11), there are two offset parameters, Ψ_{off} and y_{off}, that can both be identified using the stationary version of Equation (2.17). Stationary means all derivatives of the states y and Ψ are identical to zero, i.e. $y(t) = y_{\mathrm{stat}}$ for all t in a time interval with y_{stat}, $\psi_{\mathrm{stat}} \in \mathbb{R}$. First, Ψ_{off} has to be found through (2.18). With $\ddot{\Psi} = \dot{\Psi} = 0$ this leads to

$$\Psi_{\mathrm{off}} = \Psi_{\mathrm{stat}}. \tag{2.26}$$

All other terms cancel out. With this knowledge, the stationary case of the differential equation of y (2.19) can be analyzed, as y_{off} is dependent on Ψ_{off}. This means $\dot{\tilde{y}} = 0$.

Furthermore, $\dot{\tilde{y}}_\mathrm{f} = \tilde{y}_\mathrm{f} = 0$, as the front axis is not being considered. Canceling out all terms as described leads to

$$y_\mathrm{off} = y_\mathrm{stat} - 2l_0\Psi_\mathrm{off}. \tag{2.27}$$

The introduced state space model in (2.11) forms the foundation for the rest of this work. Furthermore, the mathematical concepts of frequency analysis, presented in Section 2.1, are used in the following chapters. The transfer functions (2.20) and (2.23) are used to identify the parameters of themselves through fits of measurement with inputs in the form of sine sweeps. The parameters of the transfer functions are then used to calculate the parameters of the state space model with the equations presented in this chapter.

Chapter 3

Simulation of the System Dynamics

To simulate the model presented in Chapter 2, it is implemented in MATLAB Simulink (2023b) [36] shown in the block diagram in Figure 3.1. As set out in Section 2.3, this model only considers the rear axis leading to $y_\mathrm{f} = 0$. Furthermore, examining the nominal values introduced in Table 3.1 shows that both Ψ_off and y_off are zero in the nominal case. Looking at the block diagram with this in mind, the transfer functions from u to Ψ and from Ψ to y can be found directly.

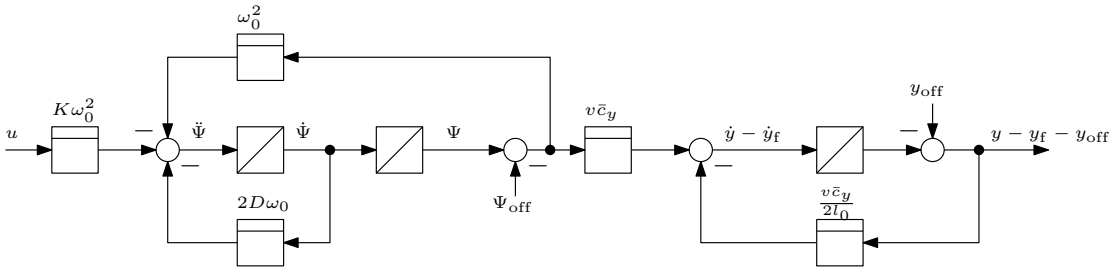

Figure 3.1: Block diagram of the state space model.

First, the simulation was used to generate Bode diagrams of the transfer functions by using the nominal values of the parameters presented in [6] and shown here in Table 3.1 and the values of the constants introduced in Table 2.1. The parameters K (2.15), ω_0 (2.13), D (2.14), and $\bar{c_y}$ (2.12) have to be calculated using their respective equations with the relevant nominal parameters.

Table 3.1: Nominal Parameters.

Parameter	**Nominal**
l_0 in m	$2.5 \cdot 10^{-1}$
δ_0 in rad	$2.4 \cdot 10^{-2}$
y_{off} in m	0
J_z in kg m^2	$8.0 \cdot 10^{-1}$
k_{c} in N/m	66.0
k_{d} in N s/m	$6.6 \cdot 10^{-1}$
Ψ_{off} in rad	0

A sine sweep, as described in Subsection 2.1.3, was used to obtain a Bode diagram from one simulation. The Bode diagrams are derived from the magnitudes A and phases φ which were obtained through the fast Fourier transform command `fft` in MATLAB [37] of the outputs Ψ and y of the simulation data. The MATLAB command `fft` uses the Fourier transform as described in Subsection 2.1.1.
Figure 3.2 shows the frequency response of the simulation data of Ψ in the range from $4 \cdot 10^{-2}$ rad/s to 100 rad/s. The magnitude takes the general shape of a PT2 element, as outlined in Subsection 2.2.2. Noteworthy are the slight increase in magnitude starting shortly before 1 rad/s, the stark decrease in magnitude at $1 \cdot 10^2$ rad/s, and the slope after the resonance peak not being -40 dB/decade. The decrease in magnitude at $1 \cdot 10^2$ rad/s is the result of numerical errors. The other two are due to the influence of the input data u on the output. Looking at the phase, it is clearly not continuous, exhibiting frequent large jumps of 360°.

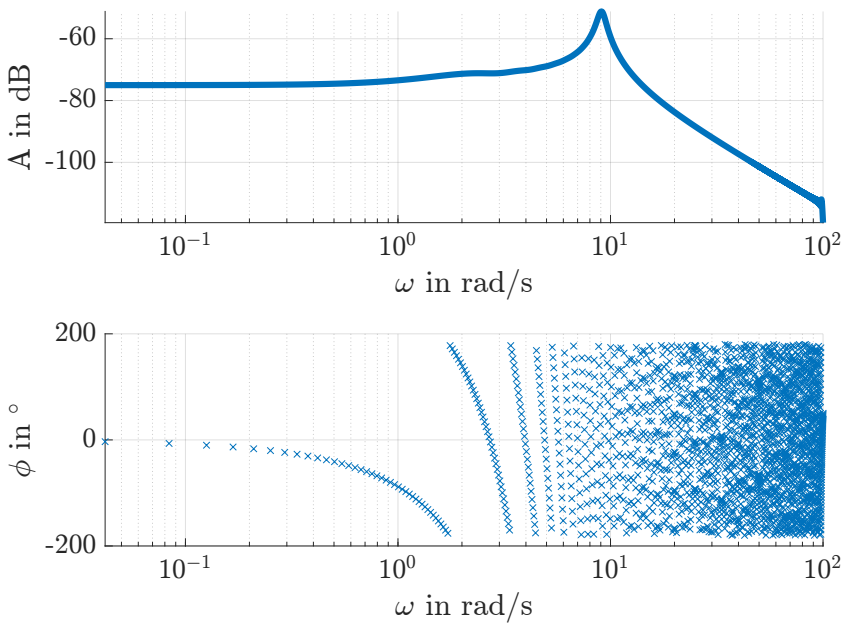

Figure 3.2: Frequency response of simulation data of Ψ.

Comparing Figure 3.3 to Figure 2.1 in Section 2.2 shows that the form of the magnitude would be expected to not have a resonance peak like a PT2 element. Although a decrease of -20 dB/decade would be expected, no decrease is seen. Both phenomena are due to the influence of the input data Ψ on the output y. Similar to Figure 3.2, the phase is

also discontinuous and displays jumps of 360°.

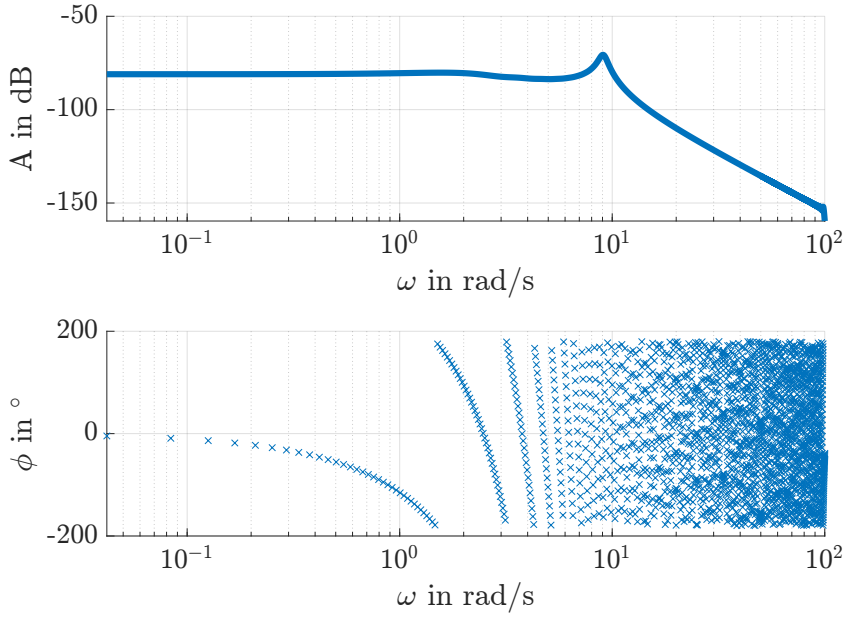

Figure 3.3: Frequency response of simulation data of y.

The conclusion from the Bode plots in Figure 3.2 and Figure 3.3 is that they have to be normalized to obtain the transfer functions. This means to divide the magnitude of the output by the magnitude of the input, leaving the gain. The phase of the input has to be subtracted from the phase of the output to show the phase shift. The resulting Bode diagrams of the normalized transfer functions are presented in Figure 3.4 and Figure 3.5 together with the Bode diagrams of the transfer functions directly determined through the nominal parameters.

The Bode diagram of the transfer function from u to Ψ in Figure 3.4 shows clear PT2 element behavior, as introduced in Subsection 2.2.2. Furthermore, it can be seen that the damping factor lies between 0 and 1, as the magnitude has a resonance peak before declining $-40\,\mathrm{dB/decade}$. Although the overall phase is now continuous with an expected phase shift from 0° to −180°, individual data points still appear to be out of phase by 360°. This problem is solved by using the MATLAB command `unwrap` [38] for the phase. The command `unwrap(P)` adjusts the phase angles in the vector P by eliminating any discontinuities. Multiples of $\pm 2\pi$ are added to the angles whenever the difference between consecutive values is greater than or equal to πrad, ensuring the jump between consecutive angles is smaller than π [38].
In addition, the Bode diagram of the transfer function of the simulation data is the same as the Bode plots of the transfer function with nominal parameters. The only difference is the set of phase data points that are shifted due to effects of the Fourier transform. As the Bode diagrams are equivalent, this validates the simulation of the model.

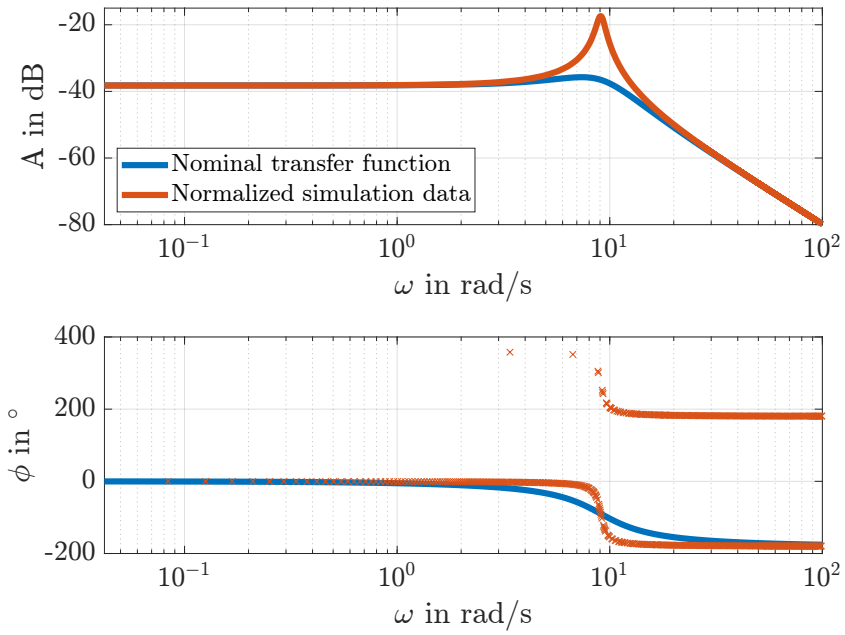

Figure 3.4: Bode diagram of transfer function of nominal values and simulation data from u to Ψ.

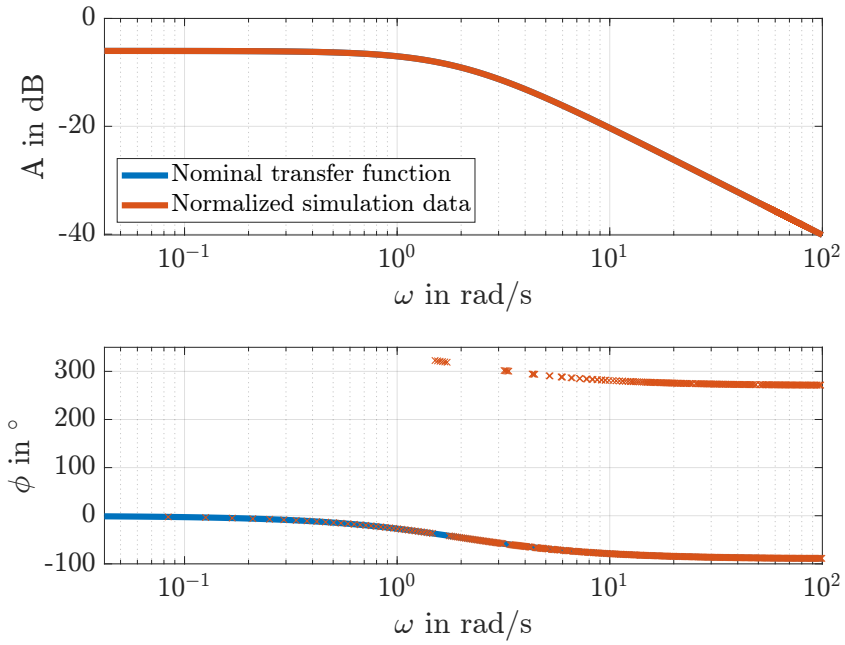

Figure 3.5: Bode diagram of transfer function of nominal values and simulation data from Ψ to y.

Figure 3.5 displays the transfer function from Ψ to y and has the expected appearance of a PT1 element, as introduced in Subsection 2.2.1. The overshoot that was visible in Figure 3.3 is removed by the normalization. Moreover, the slope after the break frequency is now $-20\,\mathrm{dB/decade}$. The phase is mostly continuous, shifting from $0°$ to $-90°$, with a few data points being out of phase, as in Figure 3.4. The phase is made continuous by using the MATLAB command `unwrap` [38].

The Bode plot of the simulation data also fits accurately over the Bode diagram of the transfer function with nominal parameters, further validating the simulation.

To allow for later use of the identified parameters instead of the nominal ones, the parameters of both transfer functions (2.20) and (2.23) described in Section 2.4 are identified through system identification of measurement data of sine sweeps. The parameters from the transfer functions are then used to calculate the parameters of the state space model, outlined in Table 2.2. In addition, the offset parameter Ψ_{off} can be identified by taking the mean of the measurement data of Ψ. Then y_{off} can be determined by taking the mean of the measurement data of y, taking into account the term including Ψ_{off}, as presented in (2.27).

In this chapter the simulation of the state space model was presented, validated, and numerical errors that occur were introduced. The focus of this thesis now moves to filtering, pre-processing, and identifying the data and this is presented in Chapter 4.

Chapter 4

Experimental System Identification and Modeling

This chapter contains the practical application of the previously introduced theory. The measurement data is Fourier transformed to identify the parameters of the state space model. The Fourier transforms of the input and output data are then used to estimate a transfer function, which, in turn, is used to identify the parameters of the state space model. The data selection and how it is prepared for the transfer function fit is presented in this chapter.

4.1 Configuration of the test rig

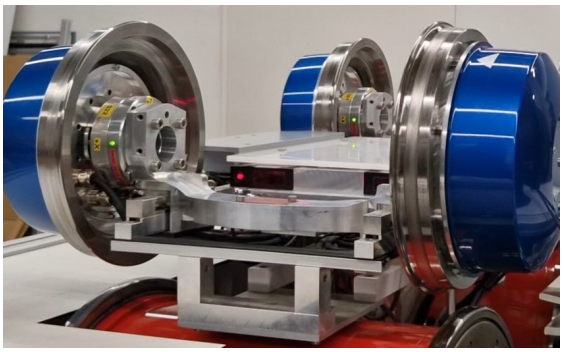

Figure 4.1: 1:5 test rig with raised axle.

The mathematical model presented in Section 2.3 only represents the rear axis. Therefore, isolated measurements of the rear axis are needed for system identification of the model. To take these isolated measurements of the rear axis, the front axis was raised to eliminate contact between the front wheels and the rollers, as depicted in Figure 4.1. As the rear axis is open-loop stable, it possible to have a sine sweep of the form (2.4) as current input and receive a stable output. The velocity of the front wheels was set to zero, so that they would not turn, when running experiments. The velocity of the rear wheels was set by the rollers, while the motor of the wheels controlled the lateral movements, as explained in Subsection 1.2.3. Additionally, the raised front and rear axis

on the rollers were manually adjusted to minimize the lateral displacement of the axis at the beginning of each experiment. This was done for multiple reasons. Firstly, to try to get the most comparable measurements by having the same starting position. Secondly, to avoid the lateral displacement of the front axis having an influence on the rear axis and thirdly, to try to minimize the contact between the flanges of the rear wheels and the roller, by having the contact points of the wheels and the roller centrally on the roller surface.

4.2 Measurement Data

For this system identification, sine sweeps, as described by (2.4) were used as current input u for the measurements. The benefit of sine sweeps is that Bode plots can be generated directly from the data, as a complete frequency spectrum is covered by one measurement. Moreover, linear systems that have a sinusoidal input produce a sinusoidal output, with only two parameters changing, the magnitude A and the phase φ [31].

A series of measurements were conducted using sinusoidal inputs at varying frequencies. For each input frequency, the system response was recorded, and a Fourier transform was applied to extract the gain at the corresponding frequency. The extracted gain values from multiple measurements were then compiled and plotted in a Bode diagram. This Bode diagram was then compared to a Bode diagram of a sinusoidal input with a frequency sweep like (2.4) to validate the direct use of a sine sweep instead of multiple measurements at different frequencies. The Fourier transform of both types of measurements directly overlap at the corresponding frequency. Thus, sine sweep measurements can be used instead of having to take numerous measurements with different frequencies. Furthermore, different frequency ranges were tested to find appropriate ranges that deliver the best results for the fits of the transfer function. First measurements showed that the break frequency of the transfer function from u to Ψ was in the range between $10\,\mathrm{rad/s} - 15\,\mathrm{rad/s}$. They also showed that noise increased drastically at frequencies larger than $80\,\mathrm{rad/s}$ for the transfer function from u to Ψ, visible in Figure 4.2a, making these measurement points not usable for accurate transfer function estimation. For the fitting of the transfer function from Ψ to y, including small frequencies starting at $1 \cdot 10^{-3}\,\mathrm{rad/s}$ turned out to be invaluable to specifically show the correct value for the stationary gain. Noise levels for this transfer function already increased at frequencies greater than $30\,\mathrm{rad/s}$, shown in Figure 4.2b. In addition, different lengths of time were tested to decide on a length of measurement that still accurately depicts the sine sweep. A further restriction was the magnitude of y, as too large amplitudes lead to flange contact. Flange contact leads to highly non-linear effects that are not in the scope of this thesis. Thus, a measurement of a logarithmic sine sweep in the range of $1 \cdot 10^{-3}\,\mathrm{rad/s}$ to $640\,\mathrm{rad/s}$ and of duration $t = 150\,\mathrm{s}$ was used as foundation for the system identification, by cutting of larger frequencies as described in Section 4.3.

The overall shape of the magnitude plots in Figure 4.2 are to be expected when compared to the Bode diagrams from the simulation that were presented in Figure 3.4 and Figure 3.5. Figure 4.2a takes the shape of a PT2 element with a damping coefficient $0 < \zeta < 1$, due to the visible resonance peak of the magnitude. Its phase shift is not in

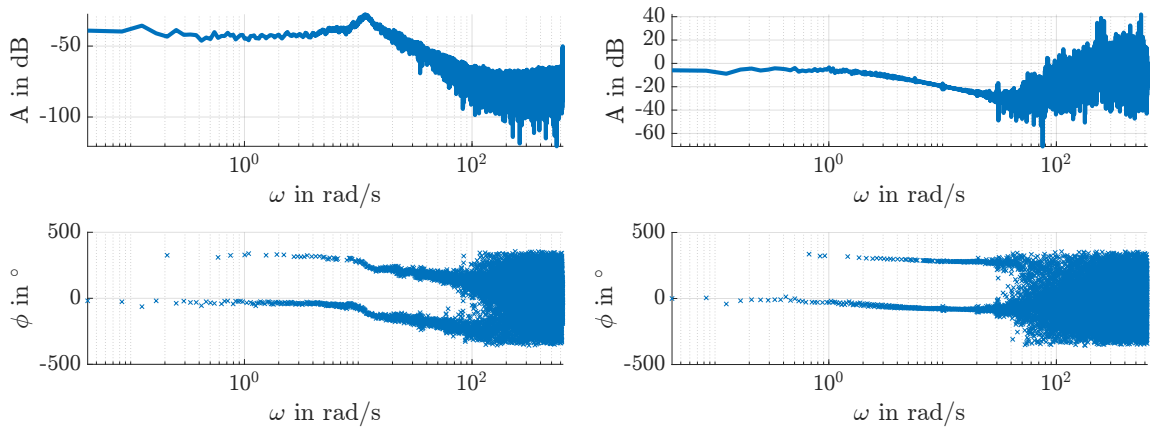

(a) Input u and output Ψ.

(b) Input Ψ and output y.

Figure 4.2: Bode diagrams of transfer functions of normalized measurement data.

the expected range and will need adjusting as explained in the proceeding Section 4.3. The expected form of the gain of a PT1 element can be seen in Figure 4.2b. Here again, the phase shift will have to be adjusted. Apart from more noise at higher frequencies, the phase shift for both transfer functions, as seen in Figure 4.2, is not in the expected range, due to the Fourier transform finding phase shift values that are out of phase by 360°.

4.3 Processing of the Measurement Data

As described in the last section, the acquired data has to be prepared to be able to be used for the system identification. For this, different measures were taken. From Chapter 3, it was expected that the measurement data had to be normalized and the phase shift had to be brought into the right range. Noise at large frequencies was unexpected, as well as having to adjust the range of the phase.

Firstly, the data was transformed using the fast Fourier transform command in MATLAB [36]. This delivers the magnitude, phase shift and frequency of the data. As already seen in Chapter 3, to receive the magnitude and phase data of the transfer functions have to be normalized. Therefore, the phase of the input is subtracted from the phase of the output. Likewise, the gain is found by dividing the magnitude of the output by the magnitude of the input. The normalized data of the transfer function from u to Ψ can be seen in Figure 4.2a and the transfer function from Ψ to y is visible in Figure 4.2b.

Secondly, as presented in Figure 4.2, both considered transfer functions have frequencies after which noise gets to large to deliver accurate results. Therefore, all data from the Fourier transforms of the measurement data relevant for the transfer function from u to Ψ were cut at the closest frequency data point to 80 rad/s, see Figure 4.3a. All data from the Fourier transform of the measurement data relevant for the transfer function from Ψ to y were cut at the closest frequency data point to 30 rad/s, depicted in Figure 4.3b.

In special cases, the Fourier transform data had to be cut to even smaller ranges, as the phase experienced jumps that were not suited for fitting. Other data was not usable for that reason, as they had regular phase jumps that made cutting the data to a range that was still usable for fitting impossible.

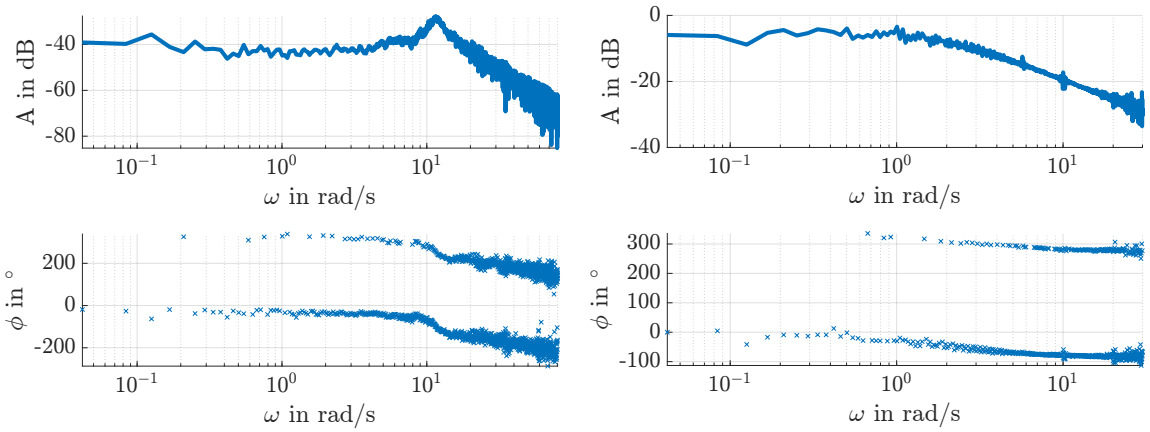

(a) Input u and output Ψ.

(b) Input Ψ and output y.

Figure 4.3: Bode diagrams of transfer functions of normalized and cut measurement data.

Like the simulation results in Chapter 3, the phase shift has to be made continuous by using the `unwrap` command in MATLAB [38].
The measurement data for both transfer functions with the use of the `unwrap` command is to be seen in Figure 4.4.

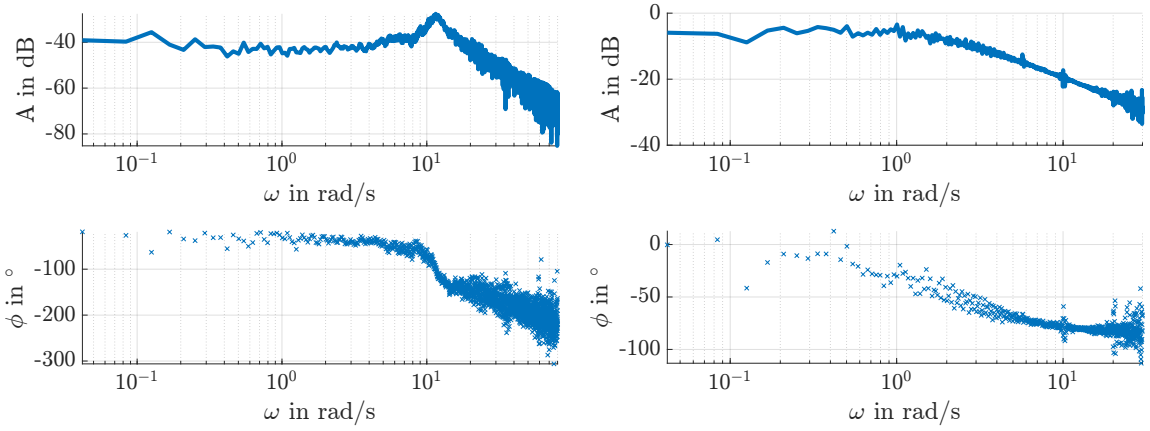

(a) Input u and output Ψ.

(b) Input Ψ and output y.

Figure 4.4: Bode diagrams of transfer functions of normalized, cut, and unwraped measurement data.

Despite having a continuous phase after using this command, the Bode plots of the phase shifts still do not look like the to be expected phase shifts of the PT elements. They often start at values other than the 0° expected value at low frequencies. Furthermore, the difference between the value of the first phase shift data points and the last are

not the expected $-90°$ for a PT1 element or $-180°$ for a PT2 element, as explained in Section 2.4. To adapt the phase shift data, first the difference between the mean of the first 15 phase shift values and the last 15 data points is found. All data points are then scaled by the factor of 180 for PT2 elements or 90 for PT1 elements divided by (mean of first 15 data points - mean of end 15 data points). To then shift the phase to start at 0°, the value of the first data point is subtracted from all phase data points. The resulting Bode diagrams are presented in Figure 4.5. They depict the adjusted measurement data that was used for the parameter identification of the transfer functions.

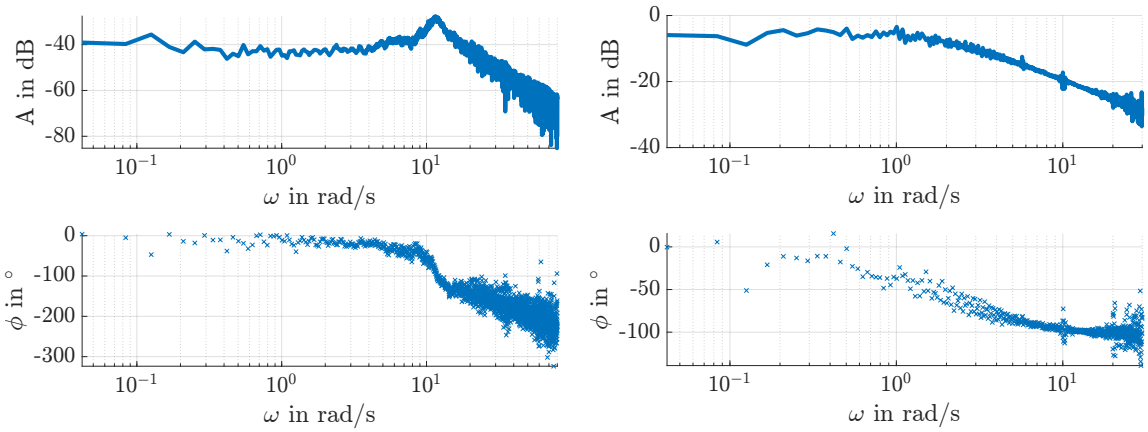

(a) Input u and output Ψ.

(b) Input Ψ and output y.

Figure 4.5: Bode diagrams of transfer functions of normalized, cut, unwraped, and adjusted measurement data.

4.4 System Identification based on Measurement Data

To use the SIT [27] in MATLAB, the input and output have to be of the form of the Fourier transform $Ae^{j\varphi}$ (2.1), with A representing the magnitude and φ the phase shift. The relevant input and output data in frequency-domain form is loaded into an `iddata` object [39] together with the sample time $T_s = 5 \cdot 10^{-3}\,\mathrm{s}$, given by the test rig, and an array containing the corresponding frequencies. The `iddata` object can then be used to estimate a transfer function using `tfest` of the SIT [27] by setting the correct number of zeros, in this case zero for both and correct number of poles. The transfer function from u to Ψ as described in (2.20) has two poles and the transfer function from Ψ to y, presented in (2.23) has one pole. The command `tfest` then yields the transfer function of the set form together with the quality of the fit, given in percent by performing the algorithm described in [40]. As described in Chapter 3, the parameters can then be identified.

Apart from using the SIT, the parameters were also fitted manually by setting the parameters of the transfer functions, k, ζ, and ω_b for the transfer function from u to Ψ and k and ω_b for the transfer function from Ψ to y by hand. For both transfer functions, first the static gain k was adjusted to fit the measurement. For transfer function from Ψ to y, the value of the static gain was then subtracted by 3 dB to find the intersection between this value and the measurement data. The frequency of the intersection was used to determine the break frequency ω_b. For the transfer function from u to Ψ, the

break frequency ω_b was adjusted to be in the right range, before changing ζ to match the size of the resonance peak. The transfer functions were then plotted against the Bode diagrams of the Fourier transform of the measurement data, by using (2.8) and (2.10) to calculate the magnitudes and phase shifts of the transfer function from Ψ to y and from u to Ψ, respectively. By performing a grid search for all parameters, the transfer functions with the most resemblance to the measurement data were be identified. The identification by hand was mostly done by fitting the magnitude plot and verifying the results through the phase plot, as the magnitude only had to be normalized, while the measurement data for the phase had to be further processed to be of use.

The higher magnitudes of the transfer function from u to Ψ are captured more accurately by the manually found transfer function than the SIT, as can be seen in Figure 4.6. In addition, the manually found transfer function from Ψ to y is visibly closer to the measurement data than the transfer function found through the SIT, as to be seen in Figure 4.7. These fits lead to the conclusion that the manually found transfer functions are even closer to the Fourier transform of the measurement data than the estimated transfer functions found through `tfest`. The SIT uses the Fourier transforms of the input and output, including both the values for the magnitude A and the phase φ to identify the transfer functions. As described in Section 4.3, the phase data had to be adjusted to make it usable. In contrast, the manual fit of the parameters could focus on accurately fitting the magnitude and then use the phase to verify the estimation instead of taking it into account for the fit. Therefore, manually fitting the transfer function to the Fourier transforms of the measurement data was able to lead to more accurate fits. As described in Section 2.5, the offset parameters are identified through the Fourier transform of the output data itself and not through the transfer functions. Therefore, the transfer functions are not relevant for the identification of these two parameters. Moreover, they have to be identified by directly using measurement data.

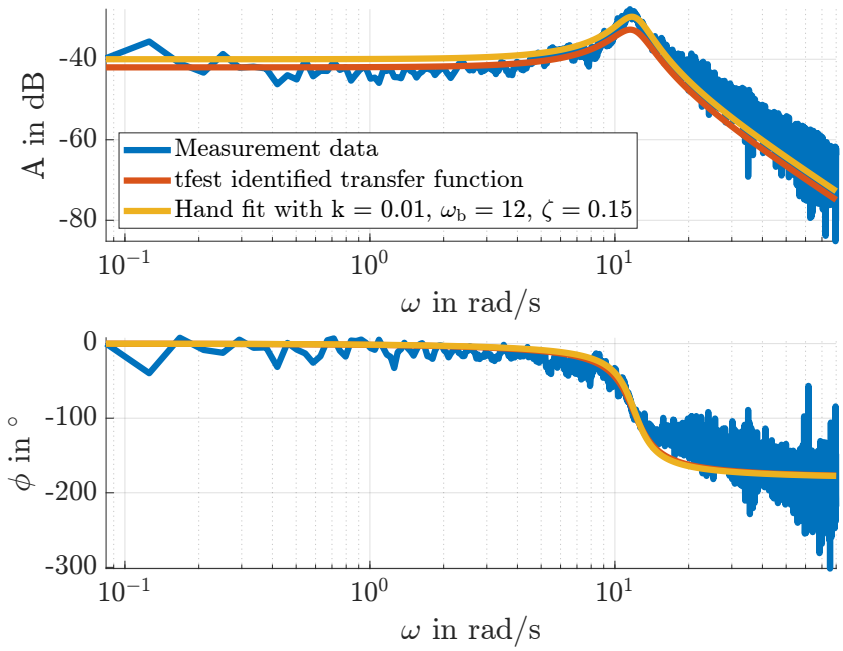

Figure 4.6: Bode diagram with input u and output Ψ comparing measurement to transfer function by tfest to transfer function of identified parameters.

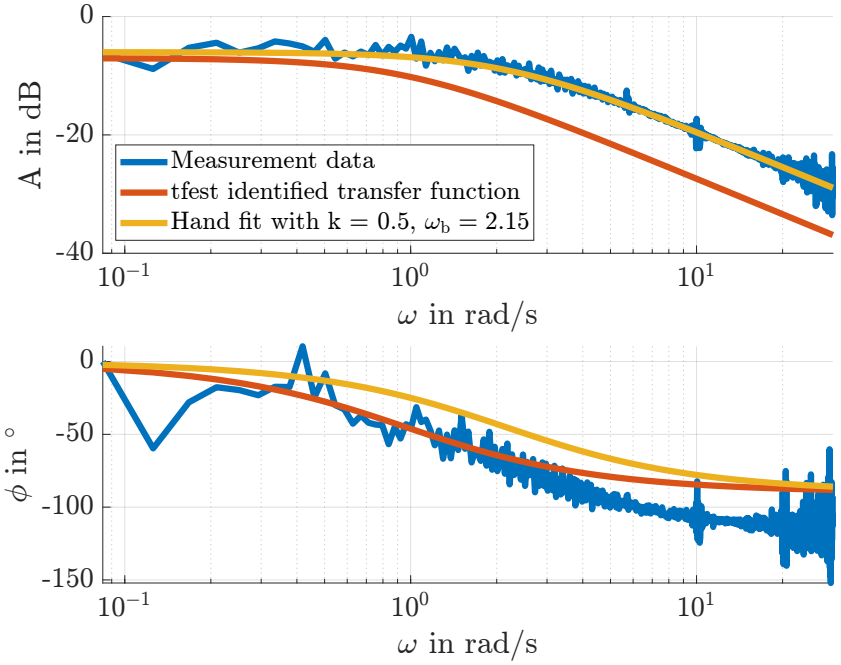

Figure 4.7: Bode diagram with input Ψ and output y comparing measurement to transfer function by tfest to transfer function of identified parameters.

With the gathered information, the parameters of the state space model can be identified with the equations derived in Chapter 2. The identified parameters of the transfer functions are used to determine the parameters of the state space model, as described in Section 2.4. The transfer function from u to Ψ is used to identify the parameters k_c, J_z, and k_d with (2.21a) – (2.21c). The transfer function from Ψ to y is used to identify l_0 through (2.24a) and then identify δ_0 with the method presented in Subsection 2.4.2. The offset parameters are calculated by taking the mean values of Ψ and y, and inserting them into (2.26) and (2.27).

4.5 Identified Parameters

The calculated parameters are presented in Table 4.1 together with the nominal values and identified ones found mostly through step responses in [6]. The identified parameter l_0 is of exactly the same value as the nominal one and the identified parameters J_z, k_c, and k_d are in the range between the nominal and identified parameters found in [6]. The identified offset parameters y_{off} and Ψ_{off} are also in the same order of magnitude as the nominal values. The only identified parameter that does not fit the range is the equivalent conicity δ_0. As described in Subsection 2.4.2, δ_0 is identified by using the MATLAB command `fzero` [34]. It describes the curving profile of the wheel with regards to the hunting motion [41]. Therefore, a negative value is impossible. Thus, from here on the nominal value is used for the simulation.

Table 4.1: Nominal vs. identified parameters.

Parameter	**Nominal**	**Identified in [6]**	**Manually Identified**
l_0 in m	$2.5 \cdot 10^{-1}$	$2.8 \cdot 10^{-1}$	$2.5 \cdot 10^{-1}$
δ_0 in rad	$2.4 \cdot 10^{-2}$	$5.0 \cdot 10^{-2}$	$-1.5 \cdot 10^{-1}$
y_{off} in m	0	$-6.0 \cdot 10^{-4}$	$1.9 \cdot 10^{-4}$
J_z in $\text{kg}\,\text{m}^2$	$8.0 \cdot 10^{-1}$	$2.8 \cdot 10^{-1}$	$5.6 \cdot 10^{-1}$
k_{c} in N/m	66.0	98.8	81.0
k_{d} in $\text{N}\,\text{s/m}$	$6.6 \cdot 10^{-1}$	21.0	2.0
Ψ_{off} in rad	0	$-1.8 \cdot 10^{-3}$	$1.6 \cdot 10^{-3}$

As the manually identified transfer functions lead to more accurate fits of the Fourier transforms of the measurement data, the parameters of the state space model found through the manually identified parameters of the transfer functions will be used from here on as identified parameters. As described above, the value for δ_0 will be the nominal value.

Chapter 5

Evaluation and Discussion of the Linear Model

To validate the identified parameters, the simulation results are compared to other sets of sine sweep measurements as well as to the full transfer function from u to y as described in (2.22). Furthermore, the results of the simulation with identified parameters are compared to the simulation with other sets of parameters. By simulating and comparing a step response, a different form of measurement is used for validation and comparison. To conclude this chapter, an outlook is given on measurements with different amplitudes leading to non-linear phenomena.

To quantify the evaluation of the identified parameters the root mean square error (RMSE) quantity is employed. It calculates the difference between the simulation data set F_i and measurement data A_i by taking the square root of the sum of the squares of the differences divided by the number of data points n. In this thesis it will be used through the MATLAB command `rmse`, which is defined by [42] as

$$E = \sqrt{\frac{1}{n}\sum_{i=1}^{n} |A_i - F_i|^2}. \tag{5.1}$$

The closer the error RMSE is to zero, the better the fit is considered.

5.1 Validation of the proposed model

5.1.1 Comparison of Simulation results to other Measurements

To validate the results of the simulation when using the identified parameters, it is directly compared to measurement data with sine sweep inputs with alternative frequency ranges. For this, the values of Ψ and y are plotted over time and the Bode diagrams are used. The Bode diagrams allow the comparison of the transmission behaviors from u to Ψ and from Ψ to y of the simulation to the measurements to validate the identified parameters relevant for the transfer functions. The measured values of Ψ and y in comparison to the data generated by the simulation is used to compare the directly

measurable values as well as validate the offset parameters Ψ_{off} and y_{off}.

To validate the identified parameters, the magnitude of the transfer functions from u to Ψ and from Ψ to y were compared to other measurements in Figure 5.1. The two sets of measurements chosen are linear sine sweeps of different frequency spectrum. They also differ in frequency spectrum to the measurements used for parameter identification. This shows that the linear model accurately depicts sine sweeps of different ranges. As the phase data of the measurements had to be adjusted to be of use, it was left out in this comparison. Figure 5.1 on the left shows that the break frequency ω_{b} of the simulation lies at the same frequency as the measurements and the damping coefficient ζ was also chosen accurately. A difference between the simulation and the measurements is the slope after the break frequency ω_{b}. The magnitude of the simulation is smaller than the measurement. Furthermore, the measurement from $6.3 \cdot 10^{-1}\,\text{rad/s}$ has large oscillations at small frequencies, making it difficult to evaluate the exact value of k. The magnitude of the Bode diagram for Ψ to y, depicted in Figure 5.1 on the right, validates the parameter identification shown in Section 4.5, as the frequency response of the simulation has the same declining slope after the break frequency ω_{b} and shows increasing noise at frequencies larger than $20\,\text{rad/s}$.

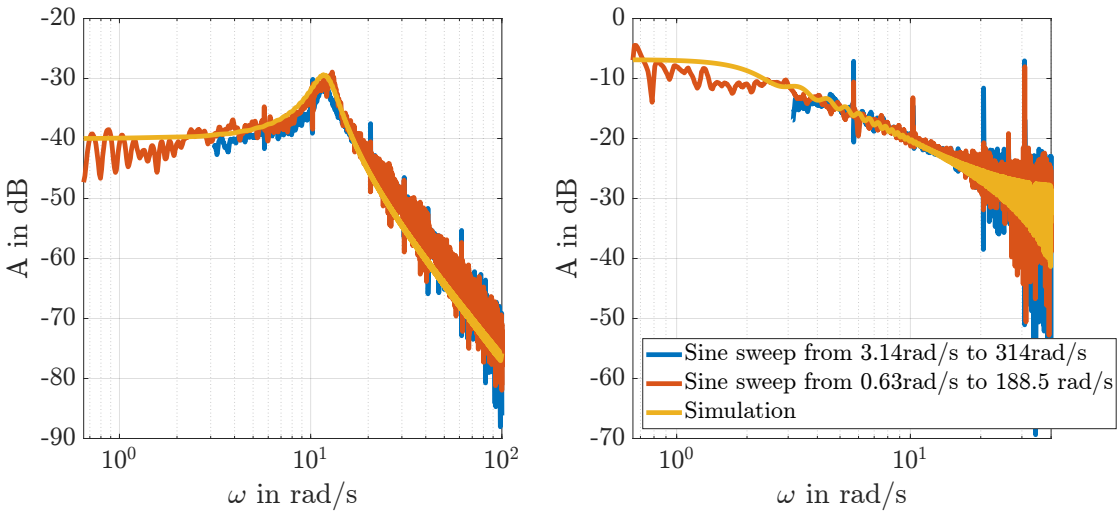

Figure 5.1: Bode diagrams for left: input u and output Ψ, and right: input Ψ and output y to validate parameters of simulation through measurements.

5.1.2 Validation of Simulation through Complete Transfer Function

The parameters were identified by fitting the transfer functions from u to Ψ and from Ψ to y. However, the complete system as described in Section 2.3 has the input u and output y. Therefore, to validate the parameters, the transfer function from u to y, presented in (2.22), will be compared to the same measurement of a sine sweep as was used to identify the parameters. Figure 5.2 depicts the simulation results and transfer function of the measurement data. One can observe that both the magnitude A and phase φ fit well over one another, showing the same effects, including the position of the break frequency and slope after the break frequency for the magnitude and similar start and end values for the phase, as well as the shift at the same speed and incline. Thus,

the simulation and the measurement show close enough results to verify the model in terms of correctly displaying the transfer behavior from input u to output y. The model is further validated by looking at the RMSE presented in (5.1) for the magnitude A and phase φ. The RMSE of the magnitude equates to $4.29 \cdot 10^{-4}$, confirming an accurate fit of the identified parameters to the measurement data. The RMSE of the phase is $5.6 \cdot 10^{-1}$. As expected, the fit of the phase is not as accurate as the fit of the magnitude, as the phase data needed adjusting before it was usable, as expained in Section 4.3.

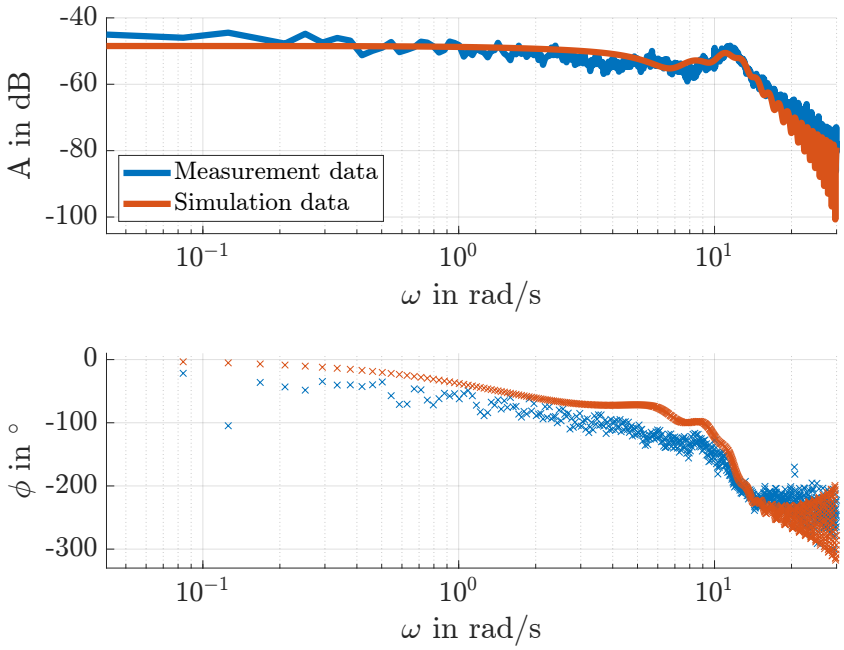

Figure 5.2: Comparison of the Bode diagram of the transfer function from u to y of the measurement vs. the simulation with identified parameter.

5.2 Evaluation and Comparison based on Step Responses

5.2.1 Comparison of Simulations with Different Sets of Parameters

As seen in Table 4.1, the parameters that were identified using frequency response are all in an expected range, apart from δ_0. The results of the simulation when using the nominal parameters, the parameters used as reference that were identified in [6], and the parameters identified through frequency response are compared in this section. It has to be noted that for the set of identified parameters, the nominal value of δ_0 was used, as described in Section 4.5.

Figure 5.3 presents the Bode diagrams for the transfer function from u to Ψ obtained from simulations with the identified parameters from Section 4.5 in comparison to the nominal parameters and the reference parameters from [6]. The most noticeable difference in Figure 5.3 is between the data with the parameters that were identified in [6] and the other simulations, for both the magnitude A and phase φ. On the one hand, the nominal parameters and the parameters that were identified in Section 4.5 show underdamped behavior, while on the other hand the identified parameters from

[6] show overdamped behavior. Comparing the parameters with underdamped behavior, the nominal parameters lead to a smaller damping coefficient and a smaller break frequency than the parameters that were identified in Section 4.5.
When comparing the phase φ, the two sets of parameters with underdamped behavior show a fast shift from 0° to −180°, as expected, while the phase of the parameters identified in [6] show a very slow shift, associated with a high damping coefficient.

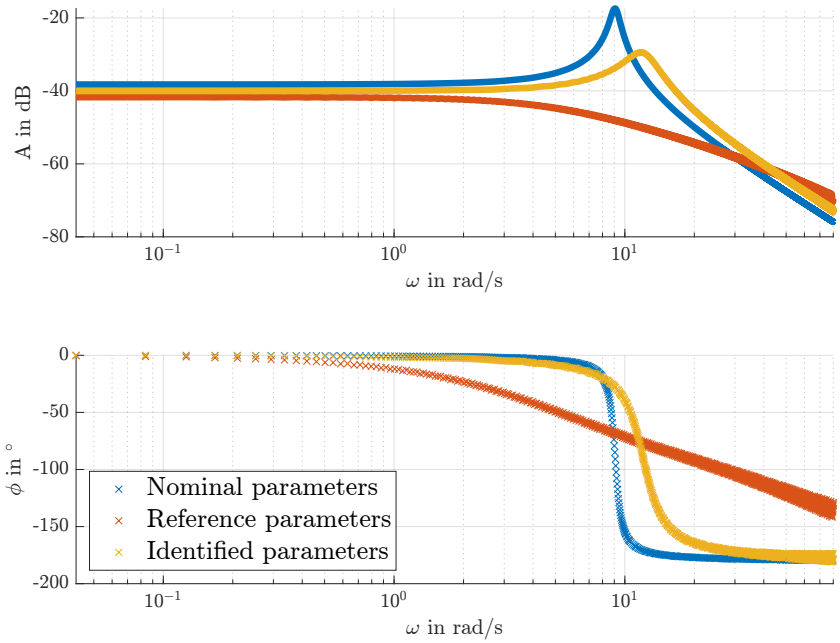

Figure 5.3: Bode diagram of simulation data of the transfer function from u to Ψ using different sets of parameters.

Figure 5.3 shows the Bode diagrams of the transfer function from Ψ to y for simulations with the identified parameters, nominal parameters, and reference parameters from [6]. In contrast to Figure 5.3, Figure 5.4 shows similar results for all sets of parameters, with the parameters from Section 4.5 being very close to the results of the nominal parameters. This was expected and will be due to l_0 being identified as the exact nominal value and using the same δ_0. The most noticeable difference can be found between the set of nominal parameters in comparison to both sets of identified parameters. Both sets of identified parameters show oscillations that increase in magnitude with higher angular frequency ω. The set of identified parameters in [6] oscillates with larger amplitudes and a different frequency than the identified parameters from Section 4.5. This will be due to numerical effects.
Looking at the phase φ, all sets of parameters show the expected behavior of shifting from 0° to −90°, but both sets of identified parameters show oscillations, with the identified parameters in [6] oscillating with larger amplitudes and a higher frequency than the set of parameters identified in Section 4.5.

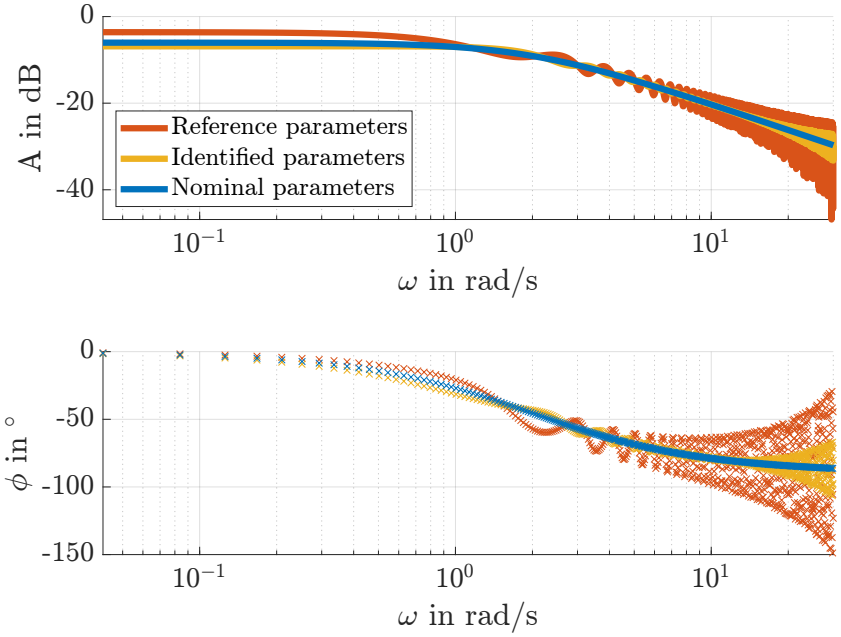

Figure 5.4: Bode diagram of simulation data of the transfer function from Ψ to y using different sets of parameters.

To evaluate the sets of parameters, they were compared against the measurement data that was used for system identification as described in Section 4.4. The RMSE, as described in (5.1), was used with the MATLAB command `rmse` [42] to quantify the quality of the parameters. Comparing the RMSE for the nominal, reference, and identified parameters shows that the set of identified parameters has the smallest error for the magnitude and phase from u to Ψ. The error is marginally smaller for the magnitude of the nominal parameters than the identified ones and the same for the phase. The results are presented in Table 5.1.

Table 5.1: RMSE of the nominal, reference, and identified parameter sets for magnitude and phase.

	Nominal	**Reference**	**Identified**
u to Ψ Magnitude	$1.4 \cdot 10^{-2}$	$7.0 \cdot 10^{-3}$	$1.9 \cdot 10^{-3}$
u to Ψ Phase	$6.7 \cdot 10^{-1}$	$9.8 \cdot 10^{-1}$	$4.9 \cdot 10^{-1}$
Ψ to y Magnitude	$3.2 \cdot 10^{-2}$	$3.3 \cdot 10^{-2}$	$3.3 \cdot 10^{-2}$
Ψ to y Phase	$5.3 \cdot 10^{-1}$	$6.2 \cdot 10^{-1}$	$5.3 \cdot 10^{-1}$

5.2.2 Simulation in Comparison to Measurement with Step Response

A simulation of a step response was taken as validation of a different type of measurement. The input was defined with the Heavyside's step function $\theta(t-a)$ and $a = 180$ from [43] as

$$u(t) = 0.6\theta(t-180) = \begin{cases} 0, & x < 180 \\ 0.6, & x \geq 180 \end{cases}.$$

Figure 5.5 shows that the simulation with reference parameters is closer to the step measurement than the simulation with identified parameters. This was to be expected, as

the reference parameters were mostly identified through measurements of step responses. The step response of the data with identified parameters show oscillations during the transient phase that are neither visible for the simulation with reference parameters nor for the measurement data. Furthermore, the offset of the identified parameters is not correct and the overall step size is too large. This shows that the set of reference parameters is able to simulate other forms of measurements more accurately than the identified parameters.

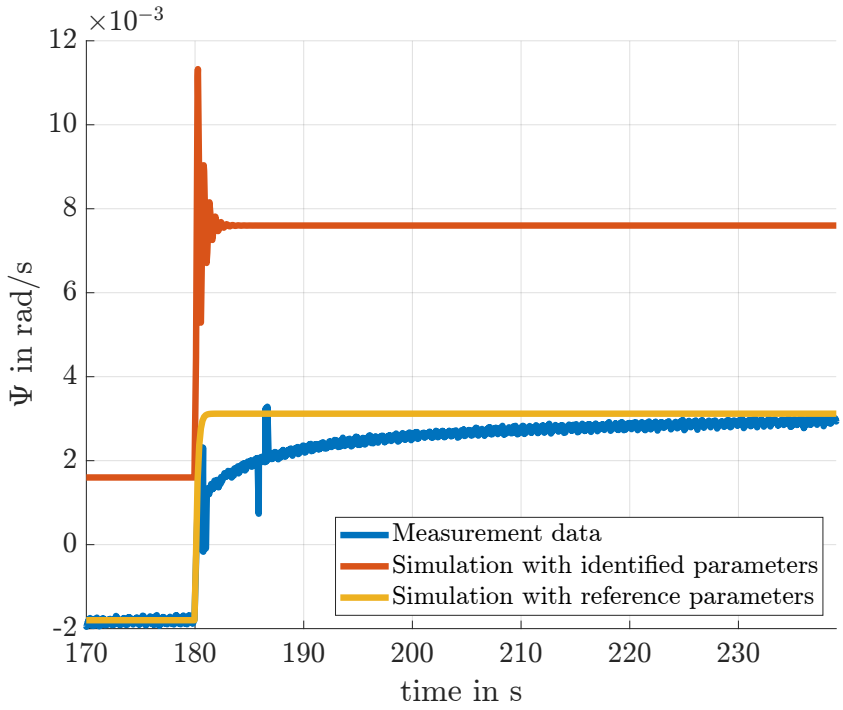

Figure 5.5: Comparison of the simulation with identified and reference parameters to a measurement step response of Ψ with a step size of 0.6.

To compare the fit of the step response with reference parameters to the step response with identified parameters, the offset between the measurements was eliminated by deducting the offset before the step from the reference parameters to the identified parameters from the identified parameter step. This made it possible to evaluate the different sets of parameters using the MATLAB command `rmse` [42] as described in (5.1). The transient phase is of particular interest, as it shows oscillations for the identified parameters. Therefore, the compared time frame was cut to between 180 s and 184 s. This resulted in an RMSE of $1.6 \cdot 10^{-3}$ for the reference parameters and $3.0 \cdot 10^{-3}$ for the identified parameters. As the reference parameters were identified mostly through step responses, it is to be expected that they fit a step response better than the parameter set identified using frequency response. In conclusion, the reference parameters from [6] are more accurate for measurements with steps. Therefore, future research may find a way to combine the reference and identified parameter sets to create a model that is able to simulate all forms of measurements.

5.3 Outlook: Frequency Responses for Different Input Amplitudes

In a linear system one would expect Bode diagrams of the same system stimulated with sine sweeps of the same frequency range but with different amplitudes to look exactly the same. The Bode diagram, as described in Section 2.1, displays the gain. This should always be the same factor, regardless of the actual value of the amplitude of the input. This also holds for the Bode plot of the phase. This displays the shift of the phase of the output in comparison to the input and is in a linear system is not dependent on and should not change with a change of the amplitude of the input.

When changing the amplitudes of the sine sweep input for the measurements, the nonlinear characteristics of the system become apparent when looking at the magnitude A of the Bode diagram of the transfer function from u to Ψ, as shown in Figure 5.6. This shows measurements of a set of sine sweep inputs of different amplitudes that used the same frequency range and the same length of measurement. As described, the expected result of a linear system would be the same magnitude plot for all measurements, regardless of amplitude.

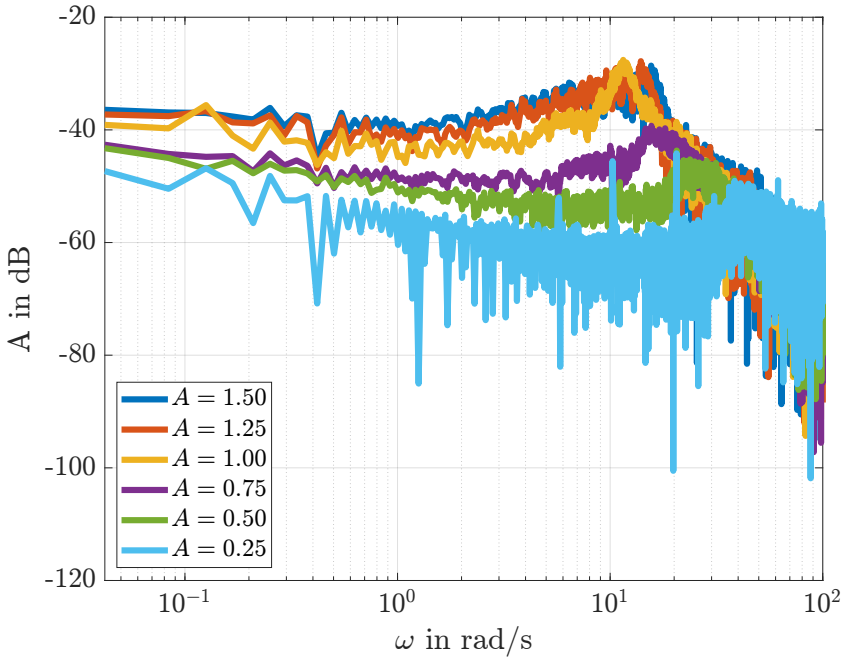

Figure 5.6: Magnitude of measurement data with inputs of different amplitudes, input: u, output: Ψ.

For the magnitude plot from u to Ψ, displayed in Figure 5.6, firstly the static gain increases with growing amplitudes. Secondly, the resonant peak occurs at smaller angular frequency with increasing amplitude up to $A = 1.00$. While the resonance peak for the measurement with $A = 0.25$ is visible at around 42 rad/s, it occurs at 26 rad/s for $A = 0.5$, at 19 rad/s for $A = 0.75$, and at 12 rad/s for $A = 1.0$. Surprisingly, the resonance peak shift back to higher frequencies for amplitudes larger than 1 and is to be seen at 12 rad/s for $A = 1.25$ and at 14 rad/s for $A = 1.50$. Secondly, the resonance

peak becomes smaller in size with decreasing magnitude, suggesting a higher damping coefficient with smaller amplitudes. Lastly, the high frequency region after the respective break frequencies appears to be the same for all amplitudes in respect to slope. The differences in magnitude suggest that the parameters k_c, k_d, and J_z change with amplitude.

The magnitude plot of the transfer function from Ψ to y, to be seen in Figure 5.7, depicts no clear differences between the measurements with different amplitudes, validated by comparing the manually fitted transfer function to the different measurements. Only the level of noise seems to change, which is due to difficulties in measuring high frequencies with small amplitudes, which is especially obvious for $A = 0.25$ at frequencies larger than 1 rad/s. This is consistent with expectations, as the parameters l_0 and δ_0, representing the distance between the wheel carrier and the middle frame and the equivalent conicity, respectively, will not change with changes in amplitude.

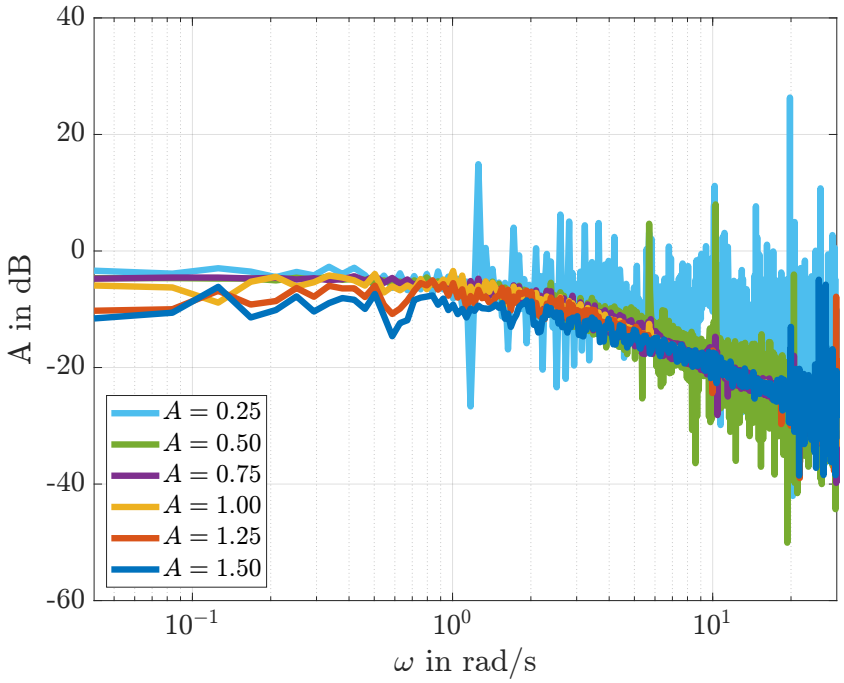

Figure 5.7: Magnitude of measurement data with inputs of different amplitudes, input: Ψ, output: y.

To understand the effects of the varying amplitudes on the identified parameters, all measurements of different amplitudes were fitted through the same method as described in Section 4.4. The results are presented in Table 5.2. The MATLAB SIT function once more did not deliver satisfying results, so the transfer functions were fitted manually to calculate the presented parameters of the state space model. As stated, l_0 and δ_0 do not change, but there are significant changes especially of k_c and k_d. The larger the amplitude up to $A = 1$, the smaller k_c and k_d. The equivalent damping parameter k_d seems to decrease in a linear manner, to be seen on the left side of Figure 5.8 for amplitudes up to 1, while the parameter for equivalent stiffness k_c seems to decrease exponentially, see middle plot Figure 5.8, but also stops changing for amplitudes larger than 1. At the same time, the offset parameter Ψ_{off}, depicted in Figure 5.9 on the left side slightly increases with increasing magnitude, while the offset parameter y_{off}, presented in Figure 5.9 on the right side seems to vary randomly from measurement to

measurement. Surprisingly, looking at the plot on the right side of Figure 5.8, J_z first increases with growing amplitude, but then declines, showing no correlation between it and the amplitude A. It is surprising that J_z changes at all, as it would be expected to stay the same, regardless of measurement input. It is assumed that k_d and k_c change due to non-linearities, while y_off could also be a result of the lateral displacement at $t = 0$.

Table 5.2: Parameters depending on amplitude.

	Nominal	**A = 1**	**A = 0.75**	**A = 0.5**	**A = 0.25**
l_0 in m	$2.5 \cdot 10^{-1}$	$2.5 \cdot 10^{-1}$	$2.5 \cdot 10^{-1}$	$2.5 \cdot 10^{-1}$	$2.5 \cdot 10^{-1}$
δ_0 in rad	$2.4 \cdot 10^{-2}$	$-1.5 \cdot 10^{-1}$	$-1.5 \cdot 10^{-1}$	$-1.5 \cdot 10^{-1}$	$-1.5 \cdot 10^{-1}$
y_off in m	0	$1.9 \cdot 10^{-4}$	$1.9 \cdot 10^{-4}$	$4.2 \cdot 10^{-3}$	$2.0 \cdot 10^{-2}$
J_z in kg m^2	$8.0 \cdot 10^{-1}$	$5.6 \cdot 10^{-1}$	$5.6 \cdot 10^{-1}$	$6.0 \cdot 10^{-1}$	$4.6 \cdot 10^{-1}$
k_c in N/m	66.0	81.0	202.5	405.0	810.0
k_d in N s/m	$6.6 \cdot 10^{-1}$	2.0	5.3	7.8	11.6
Ψ_off in rad	0	$1.6 \cdot 10^{-3}$	$-1.3 \cdot 10^{-4}$	$-7.9 \cdot 10^{-4}$	$-1.4 \cdot 10^{-3}$

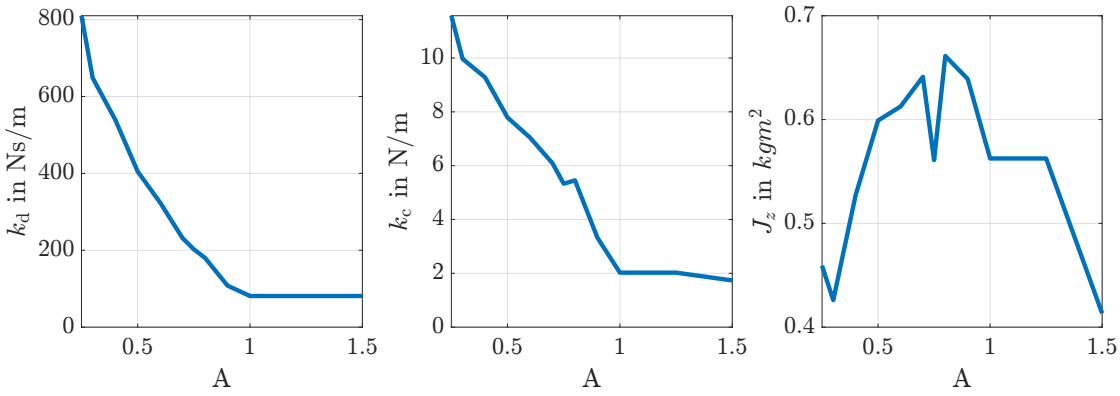

Figure 5.8: Dependence of left: Equivalent damping k_d, middle: Equivalent stiffness k_c, and right: Axle bridge inertia w.r.t yawing J_Z from amplitude A of input.

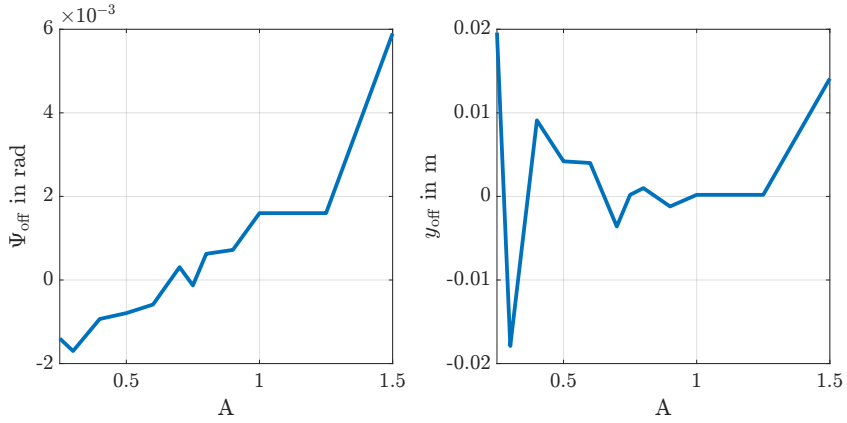

Figure 5.9: Dependence of the offset parameters left: Ψ_off and right: y_off from amplitude A of input.

Possible further research should include exploring the reason for the changing amplitudes and expanding the linear model to include the non-linear effects of the changing amplitudes by incorporating amplitude dependent parameters.

Chapter 6

Extending the Simulation Model to include Hysteresis

Chapter 2 to Chapter 4 above described the system identification of a linear model to simulate the test rig. This chapter extends that model to include the non-linear effects of hysteresis. The extended simulation is done to try and better fit the measurements. First, a general definition of hysteresis is provided, followed by an introduction to the Bouc-Wen model of hysteresis, the model applied in this thesis. The simulation model from Chapter 3 is then expanded by the introduction of a hysteresis term. The extended model is subsequently used to examine the effects of each parameter of the hysteresis term in greater detail. Finally, an attempt is made to fit the parameters of the hysteresis term to the same measurement that was previously used in Chapter 4.

6.1 Hysteresis Definition

Hysteresis in this system means that the relationship between the input and output includes memory effects. In mechanical systems, hysteresis is a natural property of materials that generates restoring forces to counteract movements and deplete energy. In these cases, hysteresis describes the memory-like behavior of inelastic materials, where the restoring force is influenced not only by the current deformation but also by the history of past deformations [44, 45].
There are different mathematical models to describe hysteresis. In this work, the Bouc-Wen model will be used, as it was used in [6]. This keeps the different forms of system identification of the same model comparable. Moreover, the Bouc-Wen model has a low number of variables, making manual fits possible. The hysteresis term of the Bouc-Wen model introduced in [6] is defined as

$$f_{\text{hyst}}(\Psi, z_{\text{Hyst}}) = \omega_0^2 \Psi - \omega_0^2 (a_{\text{Bouc}} \Psi + (1 - a_{\text{Bouc}}) z_{\text{hyst}}); \tag{6.1}$$

with z_{Hyst} described in [6] by the differential equation

$$\dot{z}_{\text{hyst}} = A_{\text{Bouc}} \dot{\Psi} - \beta_{\text{Bouc}} \left| \dot{\Psi} \right| |z_{\text{hyst}}|^{n_{\text{Bouc}}-1} z_{\text{hyst}} - \gamma_{\text{hyst}} \dot{\Psi} |z_{\text{hyst}}|^{n_{\text{Bouc}}}; \tag{6.2}$$

and the parameter $a_{\text{Bouc}} \in [0, 1]$ denotes the ratio of the stiffness between the back and front at the yield value. Furthermore, $A_{\text{Bouc}} \in \mathbb{R}$, $\beta_{\text{Bouc}} > 0$, γ_{Bouc}, and $n_{\text{Bouc}} \in \mathbb{N}$ are dimensionless parameters responsible for how the model behaves [6].

6.2 Augmentation of the Mathematical Model with Hysteresis Dynamics

Extending the mathematical model presented in Section 2.3 with (6.1) leads to

$$\ddot{\tilde{\Psi}} = -\omega_0^2 \tilde{\Psi} - 2D\omega_0^2 \dot{\tilde{\Psi}} + K\omega_0^2 u + f_{\text{hyst}}(\dot{\tilde{\Psi}}, z_{\text{hyst}}). \tag{6.3}$$

This, in turn, leads the block diagram of the state space model to be as presented in Figure 6.1. The function block for f_{hyst} contains (6.1) and (6.2) is embedded in the function block for $\dot{z}_{\text{hyst}}$.

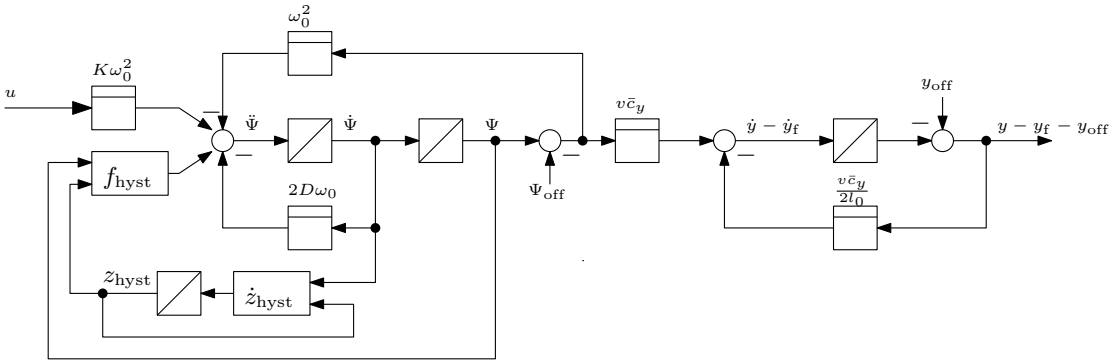

Figure 6.1: Block diagram of the state space model with hysteresis.

The hysteresis parameters identified in [6] and presented in Table 6.1 are used as reference and will be called Set R. Set R is used as starting point to understand the influence of the parameters on the transfer function.

Table 6.1: Bouc-Wen parameters. Set R was identified in [6]; Set B fits the break frequency; Set P fits the resonance peak.

Name	$\mathbf{A_{Bouc}}$	$\mathbf{a_{Bouc}}$	$\boldsymbol{\beta_{\text{Bouc}}}$	$\boldsymbol{\gamma_{\text{Bouc}}}$	$\mathbf{n_{Bouc}}$
Set R	1	$4.8 \cdot 10^{-1}$	7362	-7164	1
Set B	1	$7.5 \cdot 10^{-1}$	7400	-7400	1
Set P	$2.5 \cdot 10^{-1}$	$7.5 \cdot 10^{-1}$	7700	-7700	1

The Bode diagrams for the transfer functions from u to Ψ and from Ψ to y, depicted in Figure 6.2 and Figure 6.3, respectively, show the influence of the parameter Set R in comparison to the simulation of the linear model without hysteresis. The small oscillations found in both transfer functions with hysteresis parameters in Figure 6.2 and Figure 6.3 are noteworthy. Furthermore, Figure 6.3 shows that the hysteresis parameters do not have any influence on the break frequency of the transfer function from Ψ to y and only a small influence on its static gain. By contrast, by adding the hysteresis term the break frequency of the transfer function from u to Ψ is reduced and the static gain

increases slightly. Presumably, the hysteresis term leads to a smaller damping coefficient in comparison to the simulation of the linear model, as seen in Figure 6.2.

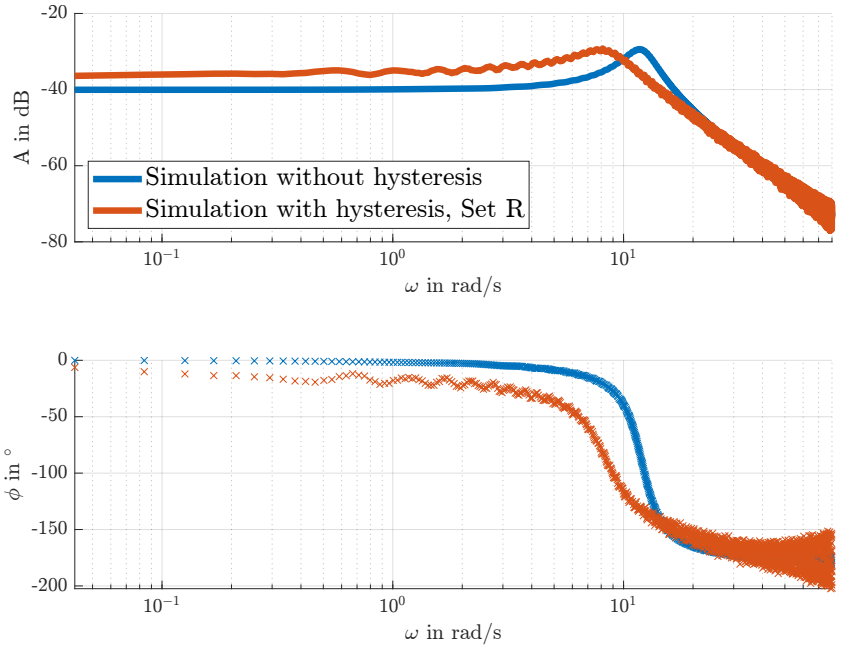

Figure 6.2: Bode diagram comparing the simulated transfer function from u to Ψ with to without hysteresis parameters.

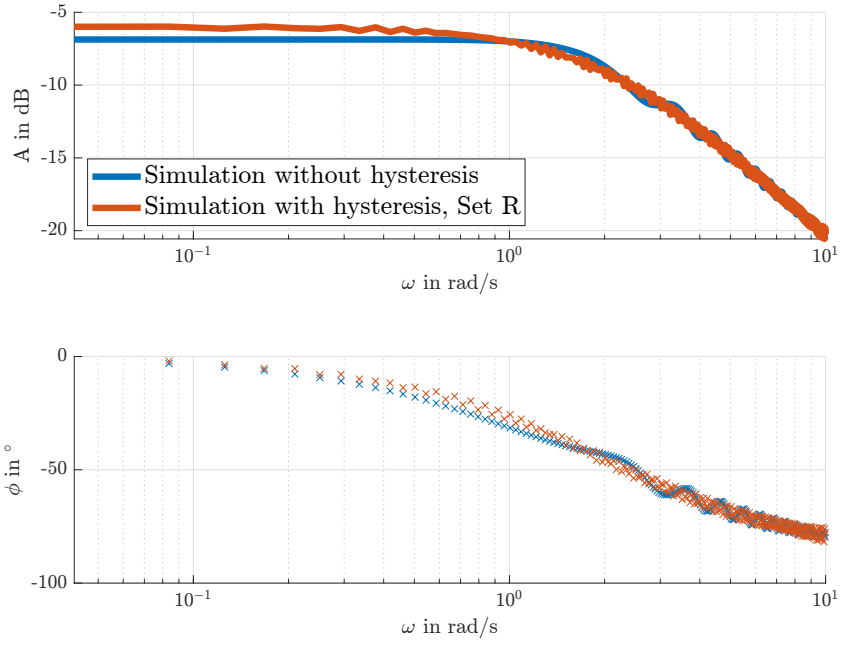

Figure 6.3: Bode diagram comparing the simulated transfer function from Ψ to y with to without hysteresis parameters.

6.3 Exploring the Effects of Hysteresis Parameters on the Model

To understand better the effects of the parameters on the simulation results, all parameters were increased and decreased individually, while keeping all other parameters at their respective reference values from Table 6.1, see Set R. The results were compared by looking at the Bode diagram of u to Ψ for Set R in comparison to the changed parameters.

This showed that β_{Bouc} has an influence on the amplitudes of Ψ and y: increasing β_{Bouc} leads to smaller amplitudes, whereas decreasing β_{Bouc} leads to larger amplitudes. At the same time, the transfer behavior of an increased β_{Bouc} lead to a larger resonance peak with a slightly smaller break frequency. Decreasing β_{Bouc} leads to a later break frequency, a smaller static gain and no resonance peak. Decreasing β_{Bouc} also leads to a smaller phase shift with more noise, while a larger β_{Bouc} results in a larger phase shift. This behavior was the same for β_{Bouc}, A_{Bouc}, and γ_{Bouc} and is therefore represented by Figure 6.4. Figure 6.5 shows that increasing a_{Bouc} leads to a shift of the break frequency to a larger angular frequency, less oscillations and a smaller static gain. Decreasing a_{Bouc} presents a smaller break frequency, but more oscillations and a larger static gain. Furthermore, a_{Bouc} has an influence on the offsets and changes the phase shift, with smaller values of a_{Bouc} also leading to more oscillations in the phase. but a smaller phase shift.

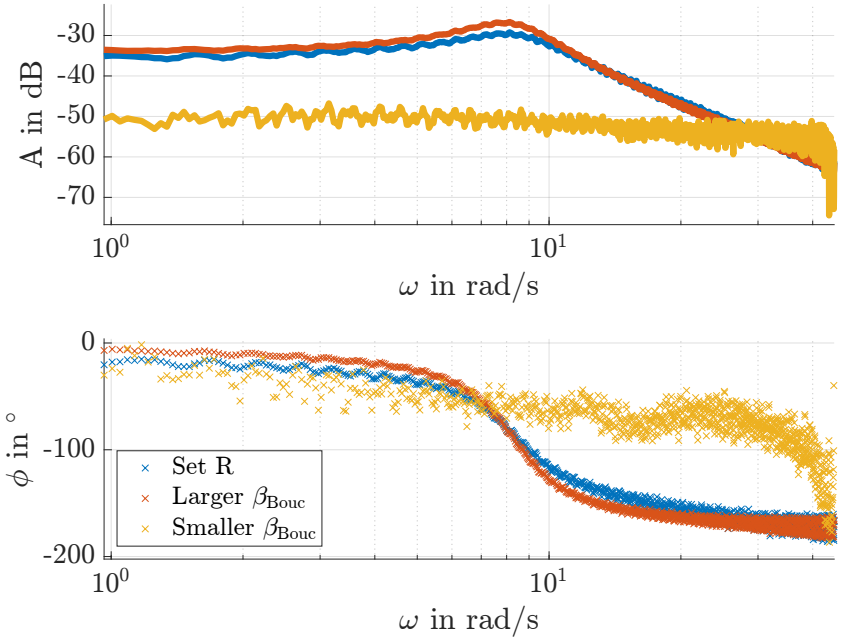

Figure 6.4: Measurement and simulation with reference hysteresis Set R in comparison to a smaller and larger β_{Bouc}.

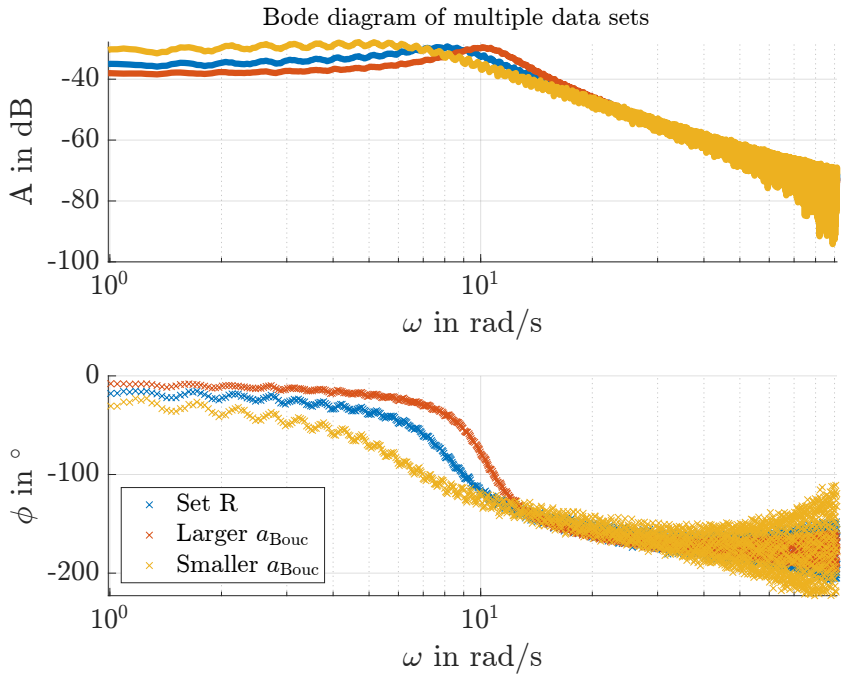

Figure 6.5: Measurement and simulation with reference hysteresis Set R in comparison to a smaller and larger a_{Bouc}.

6.4 Calibration of Hysteresis Parameters Using Measured Data

Having examined the influence of the different parameters as well as how the hysteresis parameter set R changes the transfer behavior, the parameters can now be adjusted to obtain a more precise fit of the Bode plots with hysteresis to the manual fit of the linear system presented in Section 4.4. The individual Bouc-Wen parameters are systematically increased and decreased to determine their influence on the Bode diagrams of the transfer functions from u to Ψ and from Ψ to y. Changing the hysteresis parameters only has an influence on the oscillations and the magnitude of noise at higher frequencies for the transfer function from Ψ to y, to be seen in Figure 6.7. Therefore, the focus of analyzing the influence of the hysteresis parameters is done by regarding the changes to the Bode diagram of the transfer function from u to Ψ. By increasing a_{Bouc}, the break frequency ω_{b} also increases. The hysteresis parameters β_{Bouc} and γ_{Bouc} have similar effects on the Bode diagram. Increasing them leads to a higher resonance peak, while decreasing them leads to a smaller resonance peak, but higher break frequency. A_{Bouc} has small influences on the size of the resonance peak and value of the break frequency, but the effects of β_{Bouc} and γ_{Bouc} seem to mostly outweigh the influence of A_{Bouc}. Lastly, increasing n_{Bouc} has little effect on the Bode diagram. Therefore, it was decided to set $n_{\text{Bouc}} = 1$, to simplify the hysteresis term. In conclusion, a combination of increasing β_{Bouc} and decreasing γ_{Bouc} was tested. The goal is to increase the break frequency while maintaining the size of resonance peak.

After systematically changing β_{Bouc} and γ_{Bouc}, it was decided that A_{Bouc} and a_{Bouc} will also have to be changed to achieve the desired result of fitting the transfer function with

hysteresis as close as possible to the measurement data. This poses a challenge and after testing various different combinations of these parameters, two best sets of parameters were identified, presented in Figure 6.6. It was not possible to tune manually the parameters to represent both the proper break frequency and height of the resonance peak. Therefore, two sets of parameters were found: one to fit the break frequency with a resonance peak that is too small and one set with a resonance peak close in size to the measurement but with a too low break frequency.

The values of all parameter sets are presented in Table 6.1. The measurement data used as comparison is the same data that was used to fit the parameters of the linear model in Chapter 4.
The first set, referred to as Set P, exhibits the correct height for the resonance peak, however, the break frequency is too low. The second set, designated Set B, achieves an appropriate break frequency, but the resonance peak is too small. At the same time, all sets of parameters fit the magnitude plot of the Bode diagram depicting the transfer function from Ψ to y in Figure 6.7. Due to further non-linearities, discussed in Chapter 7, the phase plot of the measurement does not show the expected shift from $0°$ to $-90°$.

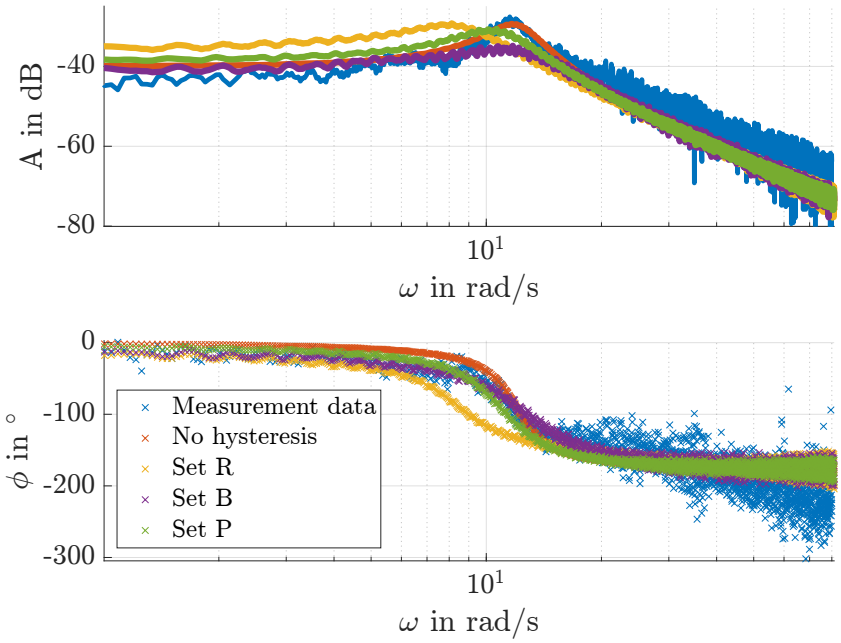

Figure 6.6: Bode diagram of measurement and simulations from u to Ψ. Set R: hysteresis values from Table 6.1, Set P: hysteresis parameters set to fit resonance peak, Set B: hysteresis parameters set to fit break frequency.

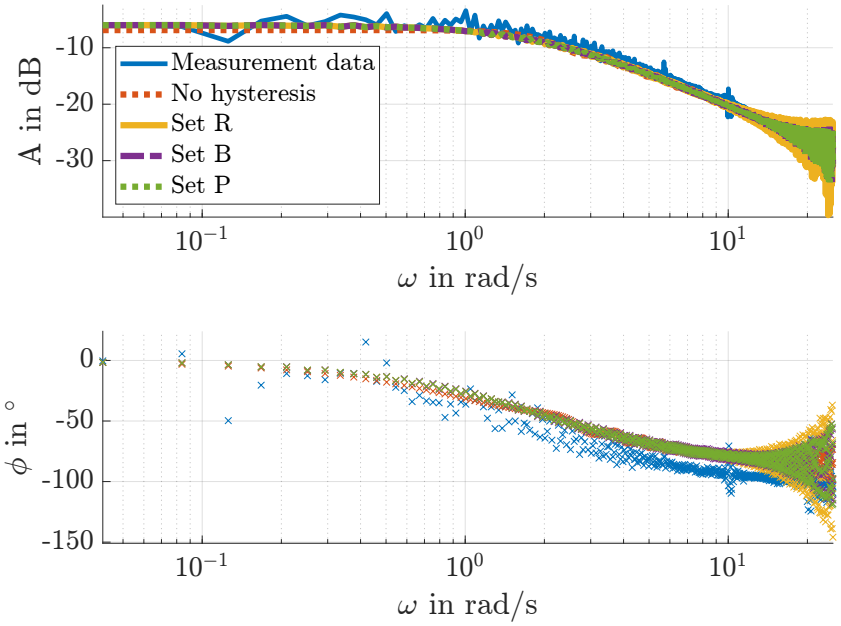

Figure 6.7: Measurement and simulation with hysteresis of left: Ψ and right: y over time. Set R: hysteresis values from Table 6.1, Set P: hysteresis parameters set to fit resonance peak, Set B: hysteresis parameters set to fit break frequency.

In Figure 6.8 the simulations of the different parameter sets are compared to the measurement data of Ψ and y over time. The amplitude of parameter Set R are too large for both Ψ and y. Set P appears to have the most accurate amplitudes of all three sets. In addition, both Set P and B have the same offsets for Ψ and y that do not fit the measurement data, but are closer than Set R.

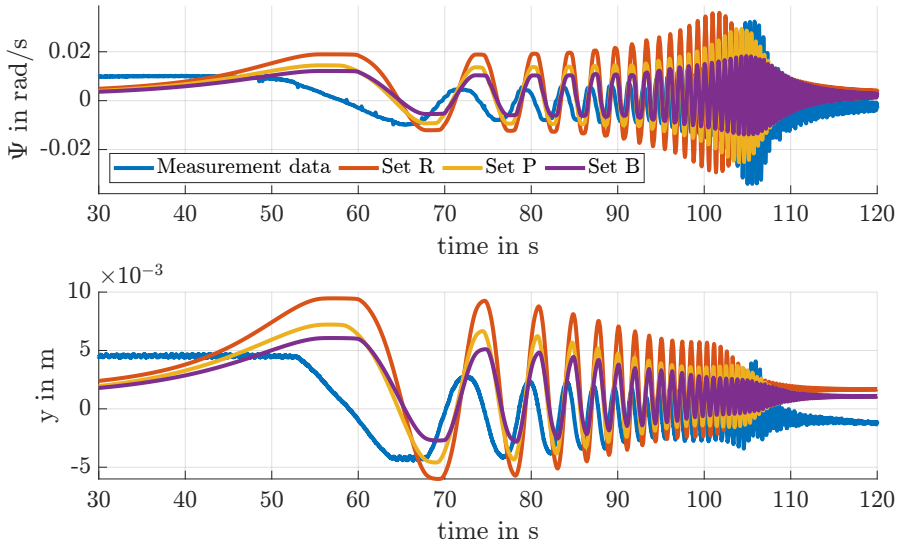

Figure 6.8: Measurement and simulation with hysteresis of top: Ψ and bottom: y over time. Set R: hysteresis values from Table 6.1, Set P: hysteresis parameters set to fit resonance peak, Set B: hysteresis parameters set to fit break frequency.

6.5 Evaluation of the Model Including Hysteresis

When quantifying the error by using the RMSE, the values presented in Table 6.2 are calculated. These show that the magnitude and phase for u to Ψ of Set P and Set B are closer to the measurement than Set R. In comparison to the identified parameters of the state space model without hysteresis from Section 4.4, the magnitude of u to Ψ of Set R, Set P, and Set B have a larger error. This is to be expected, as there was no hysteresis parameter set found that accurately fit the break frequency and resonance peak. The RMSE of the phase from u to Ψ is smaller for Set B than for the Set P or Set B and marginally smaller than for the identified parameters. The RMSE for the magnitude and phase from Ψ to y are very similar for all sets and the identified parameters without hysteresis. Although the RMSE does not give a clear direction, visually comparing the Bode diagrams presented in Figure 6.6 and Figure 6.7 leads to the conclusion that the hysteresis term, when fitted correctly, will lead to better simulation results than the linear model.

Table 6.2: RMSE of the identified parameters from Section 4.4 in comparison to Set R, Set P, and Set B for magnitude and phase.

	Identified without hysteresis	**Set R**	**Set P**	**Set B**
u to Ψ Magnitude	$1.9 \cdot 10^{-3}$	$6.1 \cdot 10^{-3}$	$3.3 \cdot 10^{-3}$	$3.6 \cdot 10^{-3}$
u to Ψ Phase	$4.9 \cdot 10^{-1}$	$5.5 \cdot 10^{-1}$	$5.0 \cdot 10^{-1}$	$4.7 \cdot 10^{-1}$
Ψ to y Magnitude	$3.3 \cdot 10^{-2}$	$3.4 \cdot 10^{-2}$	$3.3 \cdot 10^{-2}$	$3.4 \cdot 10^{-2}$
Ψ to y Phase	$5.3 \cdot 10^{-1}$	$5.5 \cdot 10^{-1}$	$5.4 \cdot 10^{-1}$	$5.4 \cdot 10^{-1}$

Overall, the hysteresis manages to depict effects that are visible in the measurements but not represented by the linear model, for example, small oscillations, varying offsets, and unexpected phase shifts. This model already represents the measurements more accurately, than the linear model.
Nevertheless, to be able to effectively use the hysteresis in the simulation further tuning will be necessary. The current sets of parameters only manage to accurately represent the magnitude of the resonance peak, represented by set P, or have the same break frequency, see set B. To manage to get both the break frequency and the height of the simulation with hysteresis to accurately represent the measurement data, further methods to tune the parameters will have to be found.

Chapter 7

Conclusion and Outlook

The objective of this thesis was to identify the parameters of the state space model, presented in Chapter 2, using the frequency responses of measurements. In this work, as explained in Section 4.2, sine sweep measurements were used. In addition, this thesis aimed to provide an initial investigation into the non-linearities present in the system.

This thesis introduced the state space model from [6] in Section 2.3. Then the transfer functions from u to Ψ and from Ψ to y were derived from the model. The state space model was implemented as simulation in MATLAB Simulink, as presented in Chapter 3. The simulation was tested by comparing the Bode diagrams obtained from a simulation with the nominal parameters to the Bode diagrams of the transfer functions with the nominal parameters. This demonstrated the numerical effects that can occur due to the simulation and Fourier transform.

The test rig setup for the measurements, described in Chapter 4, had the front axis of the test rig raised. Thus, only measurements of the rear axis were considered. Moreover, sine sweeps, as presented in Subsection 2.1.3, were introduced as input of the current for the test rig. The adjustment of the magnitude and phase obtained from the Fourier transform of the measurement data was explained. In particular the phase had to be made continuous and shifted to the expected phase shift range. From the adjusted data the Bode diagrams for the transfer functions from u to Ψ and from Ψ to y were plotted. The Bode diagrams, presented in Figure 4.5, were used for the manual parameter identification while the Fourier transforms of the input and output were used for system identification by the SIT. When comparing the Bode diagrams of the manual transfer function and the transfer function estimated by the SIT to the measurement data, it was decided that the manually identified parameters represented the measurements more accurately than the parameters found by the SIT. Therefore the manually identified parameters were used as identified parameters. Chapter 4 concludes with an explanation of how the parameters of the state space model were identified through the parameters of the transfer functions. The identified parameters were then presented.
The only identified parameter with an unexpected value was δ_0. Future research should consider a different method to identify δ_0, as the current method delivered a value that was outside the expected range.

Overall, the simulation of the linear model with the parameters of the state space model that were identified in Section 4.5 appears to be closer to the actual measurement data than the simulations with the nominal parameters or with the parameters identified in [6]. This was validated in Chapter 5. Furthermore, the linear model represents

frequency-related effects more accurately than the parameters identified in [6]. The parameters identified in this thesis will benefit simulations with sinusoidal inputs in the future. Nonetheless, the simulation of a step response is closer to the measurement data when using the reference parameters from [6] than when using the identified parameters. Therefore, future work should consider finding a parameter set that combines both sets of parameters in order to accurately represent the test rig regardless of the input form.

Nevertheless, some phenomena are not accurately represented or represented at all by the linear system, e.g., the change in Bode diagrams resulting from changing the amplitude of the input, as discussed in Section 5.3. Changing the amplitude of the input led to Bode diagrams that showed that all parameters of the transfer function from u to Ψ changed through the change of the input amplitude. It remains unclear why the Bode plots of measurement sets with different amplitudes change. This will have to be the subject of future research, as well as incorporating amplitude dependent parameters into the mathematical model and simulation. For this the parameters of the transfer function from u to Ψ for inputs of different amplitudes should be compared, to see the connection between the amplitudes and the parameters.

A further non-linear effect of the test rig is represented through hysteresis, as discussed in [6] and introduced in Chapter 6. Chapter 6 incorporated the hysteresis term into the linear model, leading to a non-linear model. The parameters of the hysteresis term were then systematically adjusted to try and find the most accurate fit of the transfer functions. Manually adjusting the parameters, unfortunately, was not satisfactory. Consequently, future research should focus on developing more effective methods for estimating the hysteresis parameters. The aim of future research should be to identify a set of parameters that accurately fits the resonance peak and break frequency. For this purpose a wide grid search of the parameters should be undertaken. With an accurate set of parameters the model with hysteresis will be more accurate than the linear model, as it shows non-linear behavior that is found in the measurements but can not be represented by a linear model.

In conclusion, the identified parameters of the linear model represent the measurement data well, but further research into different non-linear phenomena will be necessary to find a model to accurately simulate the test rig.

Appendix A

Notation

A.1 Mathematical symbols

j imaginary unit

I identity matrix

A^{-1} inverted matrix A

A^T transformation matrix of A

rect Rectangular function

A.2 Abbreviations and acronyms

DLR German Aerospace Center

IRDWs Independently Rotating Driven Wheels

NGT Next Generation Train

RMSE root mean square error

SIT System Identification Toolbox

TBP time-bandwidth product

List of Figures

List of Tables

References

[1] N. Farhat et al. “The benefits of mechatronically-guided railway vehicles: A multi-body physics simulation study”. In: *Mechatronics* 51 (2018). DOI: 10.1016/j.mechatronics.2018.03.008.

[2] T. X. Mei and R. M. Goodall. “Robust control for independently rotating wheelsets on a railway vehicle using practical sensors”. In: *Transactions on control systems technology* 9.4 (2001). DOI: 10.1109/87.930970.

[3] S. Lin et al. “Torque Distribution Control of Trains Equipped with Driven Independently Rotating Wheels for Guidance Control and Adhesion Control”. In: *International Conference on Industrial Electronics for Sustainable Energy Systems* (2023). DOI: 10.1109/IESES53571.2023.10253710.

[4] S. Bruni et al. “Control and monitoring for railway vehicle dynamics”. In: *Vehicle System Dynamics* 45 (2007). DOI: 10.1080/00423110701426690.

[5] A. Keck et al. “Estimating the wheel lateral position of a mechatronic railway running gear with nonlinear wheel–rail geometry”. In: *Mechatronics* 73 (2021). DOI: https://doi.org/10.1016/j.mechatronics.2020.102457.

[6] T. Posielek. “Modeling, System Identification, and Control of a Railway Running Gear with Independently Rotating Wheels on a Scaled Test Rig”. In: *Electronics* 13.20 (2024). DOI: 10.3390/electronics13203983.

[7] X. Deng et al. “European high-speed bogie technology review”. In: *International Journal of Vehicle Design* 79.1 (2019). DOI: 10.1504/IJVD.2019.101520.

[8] Siemens AG, Mobility Division. “ICE 4 (BR412)”. Article No. MOML-T10022-00-7600. 2016. URL: https://assets.new.siemens.com/siemens/assets/api/uuid:7fcccac1-32f9-4fb2-9763-a4584bed5cc8/data-sheet-ice4-e.pdf [visited on 3/3/2025].

[9] B. Kurzeck and L. Valente. “The mechatronic track guiding concept for the DLR "Next Generation Train"”. In: *Proceedings International Conference on Railway Bogies and Running Gears* (2010).

[10] B. Kurzeck and L. Valente. “A novel mechatronic running gear: concept, simulation and scaled roller rig testing”. In collab. with SNCF. 2011.

[11] S. Myamlin, J. Kalivoda, and L. Neduzha. “Testing of Railway Vehicles Using Roller Rigs”. In: *Procedia Engineering* 187 (2017). DOI: 10.1016/j.proeng.2017.04.439.

[12] J. Kalivoda and P. Bauer. “Roller Rig Testing at the Czech Technical University”. In: *Science and Transport Progress* 4 (64) (2016). DOI: 10.15802/stp2016/77994.

[13] V. Dybala. “Research Tools Aplicable in Designing of High-Speed and High-Power Rail Vehicles”. In: *Acta Polytechnica CTU Proceedings* 31 (2021). DOI: 10.14311/APP.2021.31.0010.

[14] Y. Michitsuji and Y. Suda. “Running performance of power-steering railway bogie with independently rotating wheels”. In: *Vehicle System Dynamics* 44 (2006). DOI: 10.1080/00423110600867416.

[15] R. Prateek et al. “Utilisation of Gyroscopic Damper to Improve Dynamic Stability and Steering in a Railway Vehicle with Independently Rotating Wheels”. In: *Advances in Dynamics of Vehicles on Roads and Tracks II* (2022).

[16] J. Wei et al. “Multiagent Reinforcement Learning for Active Guidance Control of Railway Vehicles with Independently Rotating Wheels”. In: *Applied Sciences* 14.4 (2024). DOI: 10.3390/app14041677.

[17] D. Lüdicke et al. “Development of the DLR Next Generation Train running gear research facility (NGT-FuN)”. In: *International Conference on Railway Technology: Research, Development and Maintenance* 1 (2022). DOI: https://doi.org/10.4203/ccc.1.25.3.

[18] D. Lüdicke et al. “DLR Forschungsinfrastruktur NGT-Fahrwerk (NGT-FuN)”. In: *ETR - Eisenbahntechnische Rundschau* (2021).

[19] K. J. Keesman. “System Identification: An Introduction”. Springer Science & Business Media, 2011. DOI: https://doi.org/10.1007/978-0-85729-522-4.

[20] R. Pintelon and J. Schoukens. “An Introduction to Identification”. In: “System Identification”. John Wiley Sons, Ltd, 2012. DOI: https://doi.org/10.1002/9781118287422.ch1.

[21] G. Pillonetto et al. “Deep networks for system identification: a Survey”. 2023. DOI: https://doi.org/10.48550/arXiv.2301.12832.

[22] A. Chiuso and G. Pillonetto. “System Identification: A Machine Learning Perspective”. In: *Annual Review of Control, Robotics, and Autonomous Systems* 2 (2019). DOI: https://doi.org/10.1146/annurev-control-053018-023744.

[23] H. Rake. “Step response and frequency response methods”. In: *Automatica* 16.5 (1980). DOI: https://doi.org/10.1016/0005-1098(80)90075-8.

[24] K. Küpfmüller. “Über die Dynamik der selbsttätigen Verstärkungsregler”. In: *Elektrische Nachrichtentechnik* 5.11 (1928).

[25] A. P. Sage and J. L. Melsa. “2 Classical Methods of System Identification”. In: *System Identification* 80 (1971). DOI: https://doi.org/10.1016/S0076-5392(08)62346-2.

[26] J. L. Guzmán et al. “Automatic Control with Interactive Tools”. Springer, 2023. DOI: https://doi.org/10.1007/978-3-031-09920-5.

[27] The MathWorks Inc. “System Identification Toolbox version: 23.2 (R2023b)”. Natick, Massachusetts, United States, 2023. URL: https://www.mathworks.com/help/ident/index.html [visited on 9/2/2025].

[28] T. Posielek and A. Heckmann. “Observer Design Based on Steady State and Reduced Model Information with Application to Running Gears with Independently Rotating Driven Wheels”. In: *Mediterranean Conference on Control and Automation* (2024). DOI: https://doi.org/10.1109/MED61351.2024.10566263.

[29] C. Karpfinger. “Calculus and Linear Algebra in Recipes”. Berlin: Springer, 2022. DOI: 10.1007/978-3-662-65458-3.

[30] K. Weltner et al. “Mathematics for Physicist and Engineers”. 3rd ed. Springer, 2023. DOI: https://doi.org/10.1007/978-3-662-66068-3.

[31] S. Palani. “Automatic Control Systems: With MATLAB”. Springer Nature, 2022. DOI: https://doi.org/10.1007/978-3-030-93445-3.

[32] R. Yang et al. “High-Resolution Microwave Imaging”. Springer Singapore, 2018. DOI: 10.1007/978-981-10-7138-6.

[33] L. Keviczky et al. “Control Engineering”. Singapore: Springer, 2019. DOI: 10.1007/978-981-10-8297-9.

[34] The MathWorks Inc. “fzero”. Natick, Massachusetts, United States, 2024. URL: https://www.mathworks.com/help/matlab/ref/fzero.html [visited on 2/3/2025].

[35] G. E. Forsythe. “Computer methods for mathematical computations”. Prentice-hall, 1977.

[36] The MathWorks Inc. “MATLAB version: 23.2.0 (R2023b)”. Natick, Massachusetts, United States, 2023. URL: https://www.mathworks.com [visited on 9/2/2025].

[37] The MathWorks Inc. “fft”. Natick, Massachusetts, United States, 2024. URL: https://www.mathworks.com/help/matlab/ref/fft.html [visited on 27/2/2025].

[38] The MathWorks Inc. “unwrap”. Natick, Massachusetts, United States, 2024. URL: https://www.mathworks.com/help/matlab/ref/unwrap.html [visited on 27/2/2025].

[39] The MathWorks Inc. “iddata”. Natick, Massachusetts, United States, 2024. URL: https://www.mathworks.com/help/ident/ref/iddata.html [visited on 3/3/2025].

[40] The MathWorks Inc. “tfest - Continuous-Time Transfer Function Estimation Using Continuous-Time Frequency-Domain Data”. Natick, Massachusetts, United States, 2024. URL: https://www.mathworks.com/help/ident/ref/tfest.html#btfb969_head [visited on 3/3/2025].

[41] J. Gerlici, T. Lack, and M. Kadorova. “Calculation of the Equivalent Conicity Function of the Railway Wheelset Tread Profile at the Delta R Function with a Negative”. In: *Communications - Scientific letters of the University of Zilina* 2 (2004). DOI: 10.26552/com.C.2004.2.49-56.

[42] The MathWorks Inc. “rmse”. Natick, Massachusetts, United States, 2024. URL: https://www.mathworks.com/help/matlab/ref/rmse.html [visited on 28/2/2025].

[43] L. Råde and B. Westergren. “Mathematics Handbook for Science and Engineering”. Vol. 4. Springer, 1999. DOI: https://doi.org/10.1007/978-3-662-03556-6.

[44] F. Ikhouane and J. Rodellar. “Systems with Hysteresis: Analysis, Identification and Control using the Bouc-Wen Model”. John Wiley Sons, Ltd, 2007. DOI: http://dx.doi.org/10.1002/9780470513200.

[45] M. Ismail, F. Ikhouane, and J. Rodellar. “The Hysteresis Bouc-Wen Model, a Survey”. In: *Archives of computational methods in engineering* 16 (2009). DOI: https://doi.org/10.1007/s11831-009-9031-8.